Cell Reports
Medicine

Article

Intervention with metabolites emulating endogenous cell transitions accelerates muscle regeneration in young and aged mice

Graphical abstract

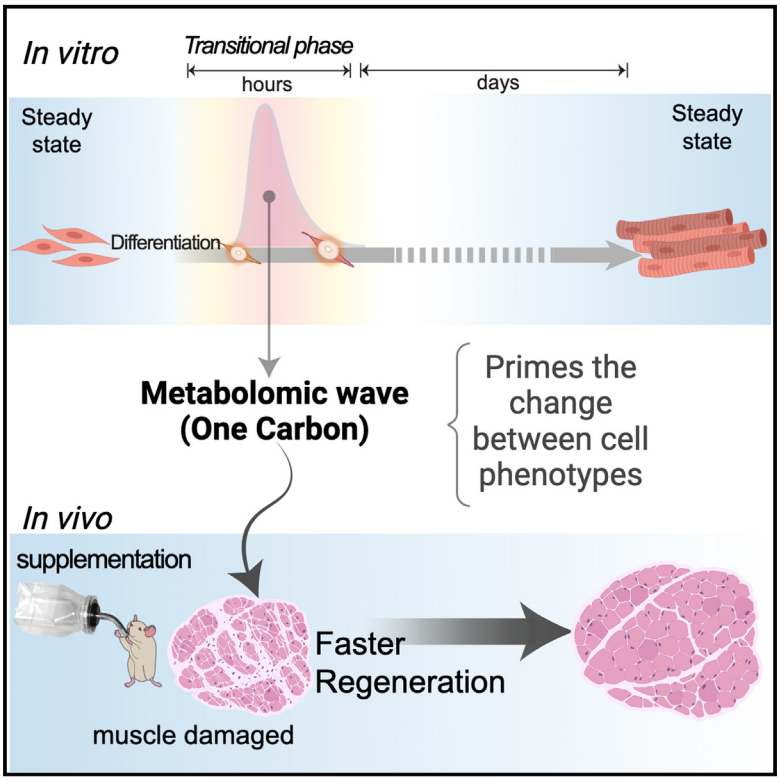

Authors

Reyna Hernandez-Benitez, Chao Wang, Lei Shi, ..., Guang-Hui Liu, Pierre Magistretti, Juan Carlos Izpisua Belmonte

Correspondence

pierre.magistretti@kaust.edu.sa (P.M.), jcbelmonte@altoslabs.com (J.C.I.B.)

In brief

Hernandez-Benitez et al. identify a metabolomic wave conserved in the early transition of cells differentiating *in vitro*, and they leverage this finding to customize an *in vivo* supplementation that facilitates the transition of cell phenotypes when needed, like in regeneration after an injury.

Highlights

- Early cell transitions in differentiation include metabolites, supporting identity changes
- Cell-transition biochemicals can be leveraged to induce plasticity
- 1C-metabolite supplementation streamlines cell-identity changes *in vitro*
- 1C-metabolite *in vivo* administration impacts acetylation genes, aiding muscle regeneration

Hernandez-Benitez et al., 2024, Cell Reports Medicine *5*, 101449
March 19, 2024
https://doi.org/10.1016/j.xcrm.2024.101449

CellPress

Cell Reports Medicine

CellPress
OPEN ACCESS

Article

Intervention with metabolites emulating endogenous cell transitions accelerates muscle regeneration in young and aged mice

Reyna Hernandez-Benitez,[1,2] Chao Wang,[2] Lei Shi,[3] Yasuo Ouchi,[2,4] Cuiqing Zhong,[2] Tomoaki Hishida,[5] Hsin-Kai Liao,[1] Eric A. Magill,[1] Sebastian Memczak,[2] Rupa D. Soligalla,[1] Chiara Fresia,[1] Fumiyuki Hatanaka,[2] Veronica Lamas,[2] Isabel Guillen,[2] Sanjeeb Sahu,[2] Mako Yamamoto,[2] Yanjiao Shao,[2] Alain Aguirre-Vazquez,[2] Estrella Nuñez Delicado,[6] Pedro Guillen,[7] Concepcion Rodriguez Esteban,[2] Jing Qu,[8,9] Pradeep Reddy,[2] Steve Horvath,[2] Guang-Hui Liu,[9,10] Pierre Magistretti,[11,*] and Juan Carlos Izpisua Belmonte[1,2,12,*]

[1]Gene Expression Laboratory, Salk Institute for Biological Studies, La Jolla, CA 92037, USA
[2]Altos Labs, Inc., San Diego, CA 92121, USA
[3]Key Laboratory of Genetic Evolution & Animal Models, Kunming Institute of Zoology, Chinese Academy of Sciences, Kunming 650201, China
[4]Department of Regenerative Medicine, Chiba University Graduate School of Medicine, Chiba, Japan
[5]Laboratory of Biological Chemistry, School of Pharmaceutical Sciences, Wakayama Medical University, 25-1 Shichibancho, Wakayama 640-8156, Japan
[6]Universidad Católica San Antonio de Murcia (UCAM), Campus de los Jerónimos, Nº 135 12, 30107 Guadalupe, Spain
[7]Clinica CEMTRO, 28035 Madrid, Spain
[8]State Key Laboratory of Stem Cell and Reproductive Biology, Institute of Zoology, Chinese Academy of Sciences, Beijing 100101, China
[9]Institute for Stem Cell and Regeneration, Chinese Academy of Sciences, Beijing 100101, China
[10]State Key Laboratory of Membrane Biology, Institute of Zoology, Chinese Academy of Sciences, Beijing 100101, China
[11]King Abdullah University of Science and Technology (KAUST), Thuwal 23955-6900, Saudi Arabia
[12]Lead contact
*Correspondence: pierre.magistretti@kaust.edu.sa (P.M.), jcbelmonte@altoslabs.com (J.C.I.B.)
https://doi.org/10.1016/j.xcrm.2024.101449

SUMMARY

Tissue regeneration following an injury requires dynamic cell-state transitions that allow for establishing the cell identities required for the restoration of tissue homeostasis and function. Here, we present a biochemical intervention that induces an intermediate cell state mirroring a transition identified during normal differentiation of myoblasts and other multipotent and pluripotent cells to mature cells. When applied in somatic differentiated cells, the intervention, composed of one-carbon metabolites, reduces some dedifferentiation markers without losing the lineage identity, thus inducing limited reprogramming into a more flexible cell state. Moreover, the intervention enabled accelerated repair after muscle injury in young and aged mice. Overall, our study uncovers a conserved biochemical transitional phase that enhances cellular plasticity *in vivo* and hints at potential and scalable biochemical interventions of use in regenerative medicine and rejuvenation interventions that may be more tractable than genetic ones.

INTRODUCTION

The dynamics and nature of cell-state transitions that lead to the establishment of cell identities, and ultimately tissue and organ function, have usually been explored during embryogenesis as well as during regeneration. Skeletal muscle tissue differentiation is among the best-studied cell-fate transition models. During physiological differentiation, a stem cell pool gives rise to muscle progenitors (or myoblasts [MBs]), which differentiate into myofibers. Complementarily, the *de novo* formation of myofibers takes place during the regeneration process after injury and is also mediated by muscle progenitors. Thus, and together with its *in vivo* accessibility, muscle represents an excellent experimental setting to uncover factors underlying cell-identity changes in both physiological and post-injury contexts.

Pioneering studies have revealed the distinctive omics signatures displayed by the steady states held by MBs and myofibers.[1,2] The changes between those cell identities are perfectly orchestrated during normal differentiation through a sequence of intermediate transitions that can be followed at different molecular levels.[3] The *in vitro* differentiation of MBs into myofibers takes at least 1 week, and available studies have explored their transitional states on a scale of days.[4] Thus, the nature of the earliest time windows associated with (or driving) the first steps critical for the activation of the transition of one cell program to another remains to be revealed. We thus hypothesized that tracking the immediate status of transitional states in differentiation could offer prospective functional candidates to best mirror an environment prone to cell-identity flexibility. With this in mind, we focused on and studied the biochemical shifts taking place in

the early-intermediate states of MB differentiation. This approach enabled us to uncover the compounds coupled to the early transitions of programs driving changes in cell phenotypes. Among them, a biochemical wave of one-carbon (1C) metabolites was detected at the initiation of MB differentiation, but it was also shared by different cell types undergoing differentiation. Subsequently, we unveil that by supplementing a few metabolites relevant to the 1C network, we can induce limited plasticity in mature differentiated cells *in vitro*. Moreover, this intervention enabled accelerated repair after muscle injury in young and aged mice. Together, our results help elucidate the role of the metabolome during the earliest stages of cell differentiation, in addition to their established role in bioenergetics,[5] exposing the sufficiency of specific biochemicals to induce cell plasticity and moderately reprogram cell fates.

RESULTS

Early transient states from MB differentiation reveal an upsurge of a specific biochemical niche

We characterized the early transcriptomic transitions from MBs into myofibers *in vitro* to detect the molecular clues that allow the switch between the two cell identities (Figure 1A). To ensure the selection of an appropriate time frame, we first detected early expression changes in some markers of the progenitor and differentiated states of muscle cells by reverse-transcription polymerase chain reaction (RT-PCR) (Figure S1A). MBs exhibited changes in gene expression as early as 1–3 h after differentiation induction, with characteristic markers of differentiation detected after 6–12 h. Based on that gene expression track, we selected appropriate time points to perform transcriptomics. We identified significant differences in global gene expression after 3 h of differentiation induction (Figure 1B). Then, we utilized Gene Ontology analysis for insights into the molecular niche of those early transitional states. Particularly, in an early time after the induction of differentiation, between 3 and 6 h, we detected a significant enrichment of pathways associated with metabolic processes, including biosynthetic and regulatory ones (Figure 1C). This observation suggested that metabolic clues may have a crucial role in preparing the intracellular niche for achieving the turning off and on of programs during cell-identity changes. Therefore, we proceeded with untargeted metabolomic analyses in an equivalent time frame.

We used an ultrahigh-performance liquid chromatography-tandem mass spectrometry platform to comprehensively identify and quantify metabolites. Changes in the abundance of each identified metabolite were assessed, and similarities between samples were computed using principal-component analyses (PCAs). We observed that the metabolome of MBs was well separated from that of their earlier differentiated counterparts (Figure 1D). Next, to identify the biochemicals essential in the intermediate transitions, we applied recurrent pattern classification (RPC), which traces the relative mean abundances of compounds over time (Figure 1E; RPC algorithms in Data S1). RPC enabled us to visualize and identify recurrent patterns of metabolite abundance, even those exhibiting subtle increases in specific windows, allowing us to classify them into cumulative, reductive, U-shaped, or bell waves and exclude them from those that did not change over time (Data S1). Of note, the bell-wave pattern concurred with the frame pointed out by the initial transcriptomics (Figures 1A–1C and S1D). Enrichment analysis of the bell pattern showed pathways such as the Warburg effect, glycolysis and gluconeogenesis, 1C-related pathways, and lipid metabolic pathways (Figure 1F).

We next analyzed additional cell types undergoing differentiation to identify chemicals that may have a broader effect on supporting early transitional niches in cells other than MBs. Thus, we screened by RT-PCR some markers on neural stem cells (NSCs) and mesenchymal stem cells (MSCs) differentiating into astrocytes and chondrocytes, respectively (Figures S1B and S1C). We then profiled the metabolomics at the appropriate times and applied the RPC strategy. In the same way, as with MBs, we detected a bell-wave pattern overlapping the early-intermediate transition (Figures S1E and S1F). Of note, we confirmed the outcome of our classification by K-means clustering and silhouette analyses (Figures S1G and S1H). Subsequently, we performed a comparative analysis on the enriched pathways. Considering the three multipotent models tested (MBs/myofibers, NSCs/astrocytes, and MSCs/chondrocytes), we found more commonalities at the intersections of transient states (bell patterns) than at other intersections (Figure 1G, compare middle vs. right or left; Table S1). Overall, this may suggest the existence of a general fingerprint supporting the partial plasticity of intermediate states.

Transient states from multipotent and pluripotent cells share a fingerprint marked by 1C metabolites

After comparing metabolomic transitions, we found methionine metabolism and spermidine/spermine biosynthesis to be the pathways shared at the bell-pattern intersection of Venn diagrams (Figure 1G, middle). Of note, these pathways are interconnected in the 1C metabolism network. We thus explored in detail the relevant shifts in metabolites after inducing differentiation in MBs, NSCs, and MSCs (Tables S2–S4), with a subsequent focus on the early-transient state (3–6 h), corroborating the significant trends of increases in several 1C metabolites (Figure S2A).

Next, we wondered whether cells with higher levels of differentiation potential, such as pluripotent cells, could have similar readouts. We thus utilized ZHBTc4 embryonic stem cells (ESCs), a well-characterized line that efficiently changes its identity toward a trophoblast phenotype,[6] to measure the relative levels of two central 1C metabolites, methionine and S-adenosylmethionine (SAM). We found that both metabolites increased during the intermediate state identified by crucial trophoblasts markers (Figure S2B). Likewise, we explored the early transitional state during human ESC differentiation into cardiomyocytes. Consistently, we corroborated an upsurge of methionine and SAM during the early-intermediate state (Figure S2C). Thus far, our results suggest that biochemicals from the 1C network represent potential metabolites that mark the intermediate flexibility not only of MBs but also of other multipotent and pluripotent cells.

A synthetic 1C niche induces a discrete progenitor-like profile in myofibers

The transitional 1C state might mirror the metabolomic requirements of any other cells confronting a change in their

CellPress
OPEN ACCESS

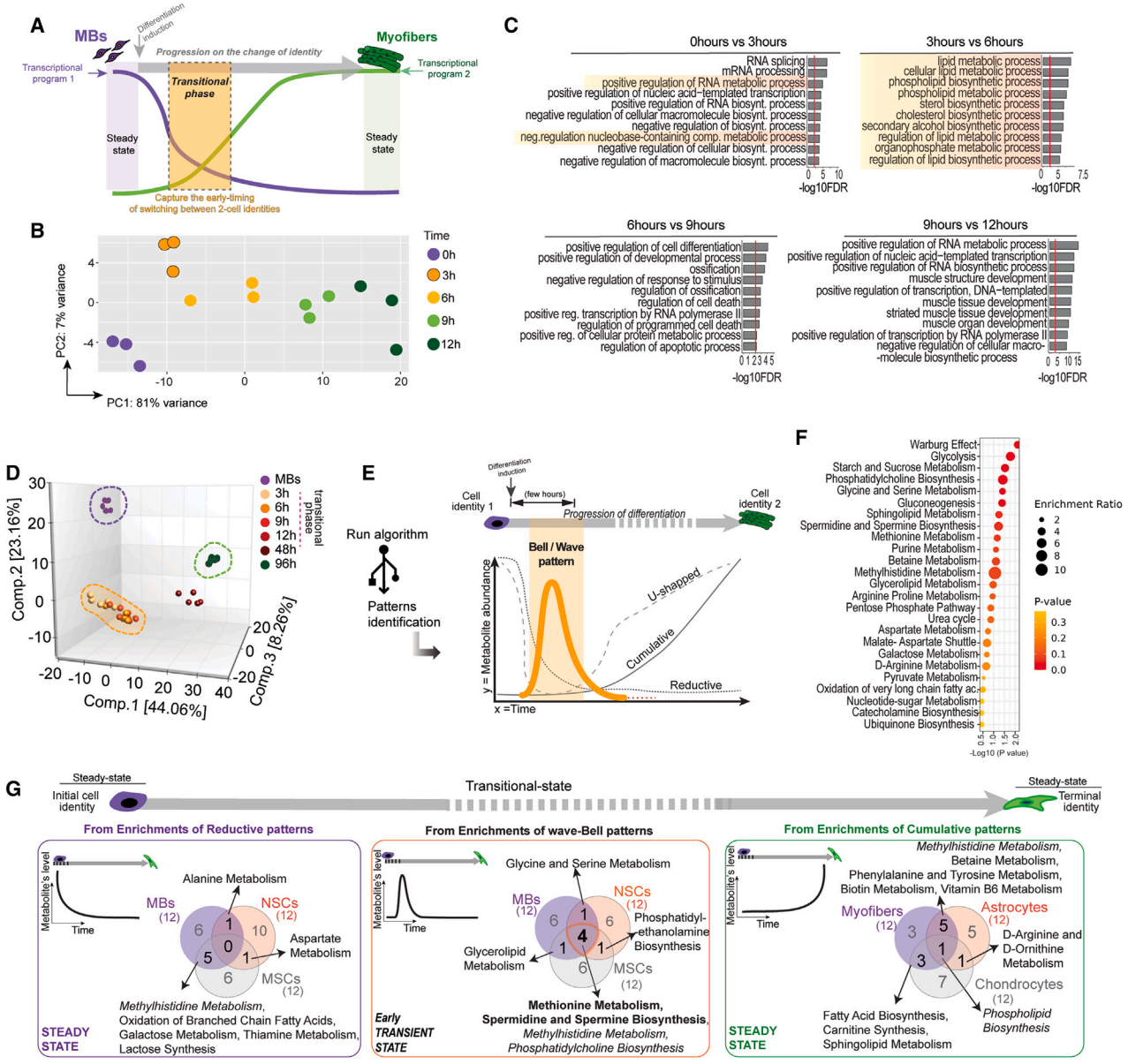

Figure 1. Identification of biochemical transitional states between myoblasts (MBs) and myofibers

(A–C) Transcriptomic analysis during the early transitional states between MBs and myofibers *in vitro*. (A) The timing of potential interest to identify the switching between transcriptional programs of two cell phenotypes. (B) Principal-component analysis (PCA) of transcriptomics at the indicated time points. (C) Gene enrichment analyses. Transcriptomic profiles were obtained by bulk RNA-seq; each sample is represented by single dots (n = 3).

(D–F) Metabolomic transitions between MBs and myofibers *in vitro*. (D) Analysis of fingerprint of the immediate populations differentiated from MBs represented in PCA. Overlapped in yellow over the PCA are the intermediate points during differentiation. Each dot represents a replicate (n = 5). (E) A schematic representation of patterns identified regarding the abundance of individual metabolites over time. The bell-shaped pattern represents an early wave of metabolites that temporally fit with the intermediate transitional populations differentiated from MBs. Enrichment analysis of the bell-patterned metabolites MBs is in (F). Analyses derived from n = 5 per time collected and per cell type.

(G) Intersections of the metabolic pathways prevalent at the initial, transitional, and terminal states of three progenitor cell types. MBs, neural stem cells (NSCs), and mesenchymal stem cells (MSCs) undergoing differentiation into myofibers, astrocytes, and chondrocytes, respectively. Venn diagrams show the intersection of the top 12 pathways derived from the enrichment analyses of reductive, bell-shaped, and cumulative-patterned metabolites corresponding to initial, transitional, and terminal states for each cell type (left, middle, and right, respectively). See the list of pathways in Table S1. Illustration tracks the change in the progression of differentiation (top horizontal gray arrow). A small inset at the top left of each Venn diagram exemplifies the type of pattern that produces the associated enrichment results. Note the commonalities derived from enrichments of the early-wave bell pattern in the central intersection in the middle image. Enrichments were obtained by MetaboAnalyst, only with metabolites having identifiers in the Human Metabolome Database (HMDB ID). Enrichments derive from data of n = 5 per time point and per cell type.

See also Figure S1, Table S1, and Data S1.

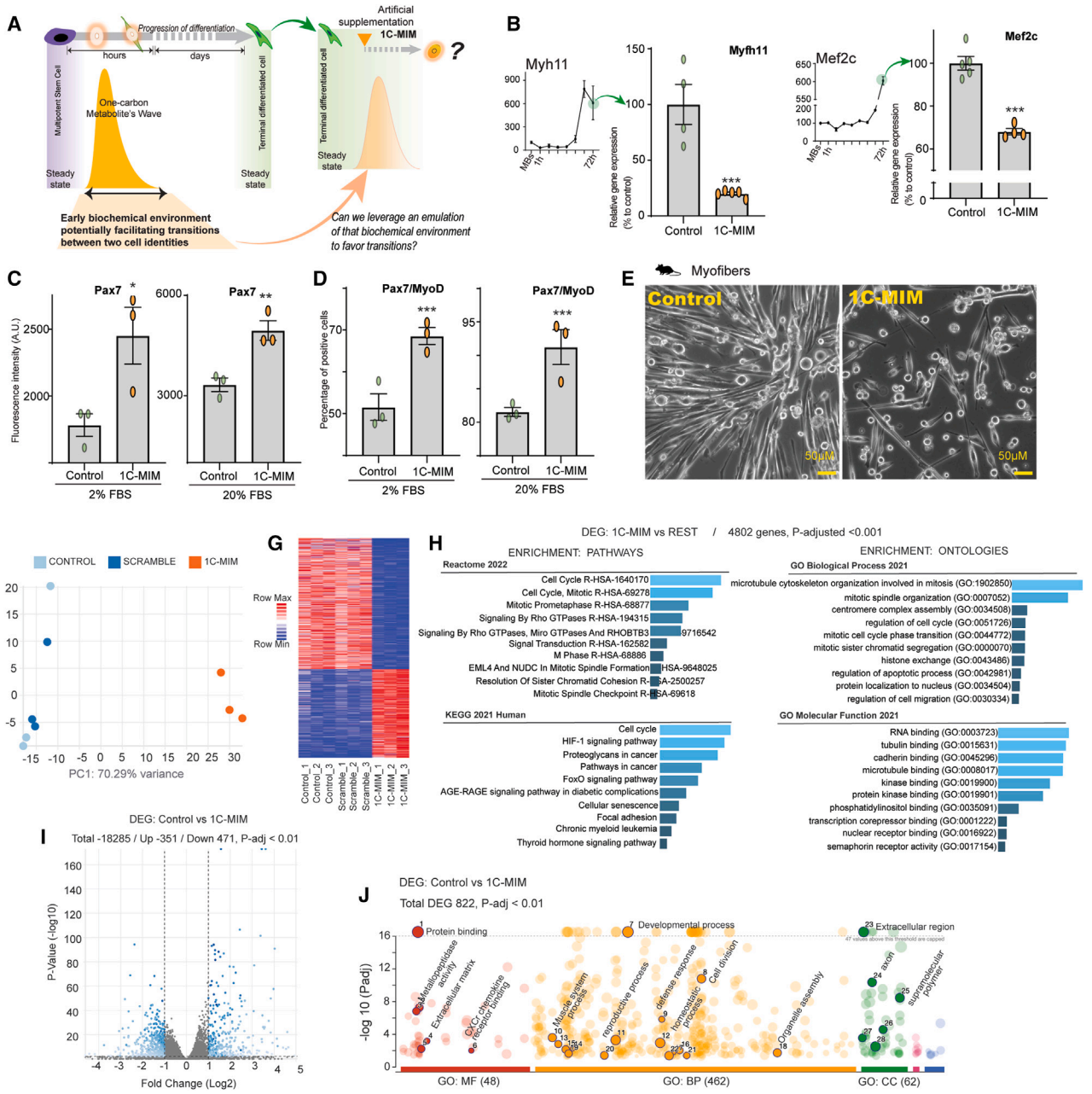

Figure 2. Mirroring the biochemical transitional niche evokes the reduction of differentiation marks on mature cells

(A) Schematic representation of the supplementation of metabolites to partially imitate a 1C (one-carbon) wave with 1C-MIM (metabolite induction medium) over a terminally differentiated steady state. Note that the 1C-MIM represents an artificial intervention to be added in mature cells that do not have a 1C wave.

(B) Effects on the supplementation of 1C-MIM over the differentiation markers of myofibers *Myfh11* (on the left) and *Mef2c* (on the right). Expression evaluated by RT-PCR. Bars represent the gene expression levels on differentiated control myofibers or those exposed for 3 days to the supplementation. Top left insets show the levels observed during differentiation. The gene expression of genes of interest was normalized with the geometric mean of at least two housekeeping genes (from *Actb*, *Gapdh*, and *Nat1*) and then normalized vs. control condition. Each dot represents an independent sample, n $\geq$ 3, with means ± SEM. The differentiation level at 72 h (bars control) is normalized to 100% to evaluate the reduction induced by 1C-MIM, where differences compared to control are significant at ***p < 0.001.

(C and D) Effects on the supplementation of 1C-MIM over the progenitor markers of myofibers Pax7 and MyoD. Protein expression levels were evaluated by immunofluorescence in myofibers exposed to different concentrations of serum; differences compared to control are significant at *p < 0.05, **p < 0.005, and ***p < 0.001.

(E) Representative images of *in vitro* control myofibers and those 3 days after the treatment with 1C-MIM. Note: a fresh feeding was done to improve the quality of the photograph; scale bar: 50 µm.

(legend continued on next page)

identity. Therefore, we treated differentiated myofibers with the *a priori*-selected biochemicals that are relevant for the 1C network, including methionine, threonine, glycine, putrescine, SAM, and cysteine (refer to STAR Methods for details on the stability and permeability of chemicals used). These molecules were selected as representatives of the 1C network prevalent across the transitional states of the several cell types presented above (Figure 2A). Because of the type of metabolites involved, we named the cocktail 1C-metabolite induction medium (1C-MIM). To get a proper customization dose effect, we exposed MB cultures to a range of concentrations of each metabolite and quantified viable ATP-metabolic active cells (Figure S3A). Orthogonally, we tested the effects of different concentrations of single and combinations of metabolites in astrocyte cultures (Figures S3B and S3C). Once the concentrations to compose 1C-MIM were chosen, a battery of control parameters were performed. Those included the viability of cultures exposed to individual metabolites and the cocktail at different times, the measurement of pH, and the levels of proteasome activity, which were tracked to verify that the effects were not due to a general loss of fitness (Figures S3D–S3H).

Next, we explored whether the artificial niche created by 1C-MIM could drive discrete reprogramming in differentiated myofibers. This was based on the premise that the intermediate transition between MBs to myofibers has an intracellular niche briefly populated by 1C-related metabolites (Figure 2A). We found that myofibers exposed to 1C-MIM exhibited downregulation of the gene expression of mature cell markers *Myh11* and *Mef2c* and recovered the protein expression of *Pax7* associated with the progenitor state (Figures 2B–2D). Because we observed a change in morphology, we validated that all cell cultures lysed for downstream analyses had at least 85% cell viability at the time of collection, eliminating the possibility that reductions in expression were derived only from mortality (Figures 2E and S3D). MB/myofiber differentiation depends on serum levels; therefore, we tested 1C-MIM at two different serum concentrations, 2% and 20% (Figures 2C and 2D). We also tested the 1C-MIM cocktail without serum in other cell types (astrocytes and chondrocytes and in additional cell types from mice and humans; see comments about this small screening in the discussion); in all these conditions, we confirmed effects like those observed in myofibers independent of serum presence (Figure S4). Of note, current strategies handled by conventional reprogramming require reduced serum or serum-free media.[7,8] Therefore, our results suggest that 1C-MIM induces in differentiated somatic cells some attributes of the corresponding progenitor state.

1C-metabolite supplementation modulates cell cycle and favors reprogramming responsiveness *in vitro*

To explore the action of 1C-MIM on myofibers, we used the *in vitro* model of C2C12. Briefly, C2C12 were differentiated by serum reduction and then exposed for 3 days to 1C-MIM or a scramble metabolite combination (mix of six metabolites non-directly related to 1C metabolism). Then, we performed RNA transcriptomics analysis. The scramble combination presented a similar profile of gene expression to the control of myofibers untreated (Figures 2F and 2G). Orthogonal results by RT-PCR in astrocytes confirmed that applying the scramble combination did not repress the expression of differentiation markers, nor did it increase the progenitor markers (Figures S3E–S3F). The differential gene expression analysis from 1C-MIM-treated myofibers vs. the rest (control and scramble) enriched cell-cycle-related pathways and cytoskeleton ontologies (Figure 2H). The 1C-MIM-treated myofibers exhibited 822 differentially expressed genes (DEGs) to their parental untreated control (Figure 2I). Among the top upregulated genes by 1C-MIM was *Mmp13*, a contributor for skeletal muscle regeneration and critical for MB migration,[9] several metalloproteinases, kinases, and genes from fetal muscle development like *Stc1*[10] (Figures 2I and 2J).

Similar deductions were derived from the transcriptomics on 1C-MIM-treated astrocytes, where the profile was closer to the progenitor NSCs and exhibited regulation of cell cycle, and cell-migration-related processes were differentially regulated between astrocytes and MIM astrocytes (Figures 3A–3C). Of note, we validated the acquisition of an intermediate-like state in the 1C-MIM-treated astrocytes. This was done by comparing the DEGs in 1C-MIM-treated astrocytes to the intermediate-NSC-like state formerly reported for the partially reprogramed astrocytes[11] and evidenced that both sets share 446 genes that, in congruence with the above results, functionally enrich cell-cycle processes (Figures S5A–S5E). Overall, the treatment of *in vitro* cells with 1C-MIM modulates the cell cycle, which, in agreement with the literature, is one of the immediate responses to the change of cellular states during cell-fate specification and reprogramming.[12,13]

To explore whether the 1C-MIM-induced state may increase responsiveness to specific differentiation factors, we infected mouse MSCs with *MyoD*, a well-characterized myogenic transcription factor, and evaluated the conversion efficiency toward myofibers when combined with 1C-MIM (Figure 3D). In this model, MyoD expression is proportional to the linked GPF+ signal, whereas successful transdifferentiation is measured thereafter by MF20, which stains differentiated muscle fibers. We observed that 1C-MIM not only increased the efficiency of conversion up to 5-fold but also accelerated the cell conversion,

(F–J) Transcriptional characterization of the identity acquired by myofibers after 1C-MIM supplementation. (F) PCA map of control untreated myofibers, myofibers treated with a scramble combination of metabolites non-related directly to 1C (see main text for details), and 1C-MIM-treated myofibers. Transcriptomic profile obtained by bulk RNA-seq. (G) Hierarchical cluster analysis (HCA) performed using a Euclidean distance metric comparing gene expression profiles; red to blue color gradient indicates higher to lower expression. (H) Gene set enrichment analyses of the DEGs between 1C-MIM myofibers vs. the rest (control and scramble); to the left are enrichments for pathways, and to the right is enrichment for ontologies. (I) Volcano plot representations of differentially expressed genes (DEGs) at the comparison myofibers control to 1C-MIM. DEGs are represented by dots (adjusted p value [p-adj.] < 0.01). Blue dots indicate significantly upregulated and downregulated genes. Gray dots indicate not significant genes. (J) Enrichment analysis by gProfiler of DEGs included 471 downregulated and 351 upregulated considering p-adj. < 0.01.
See also Figures S2–S4 and Tables S2–S4.

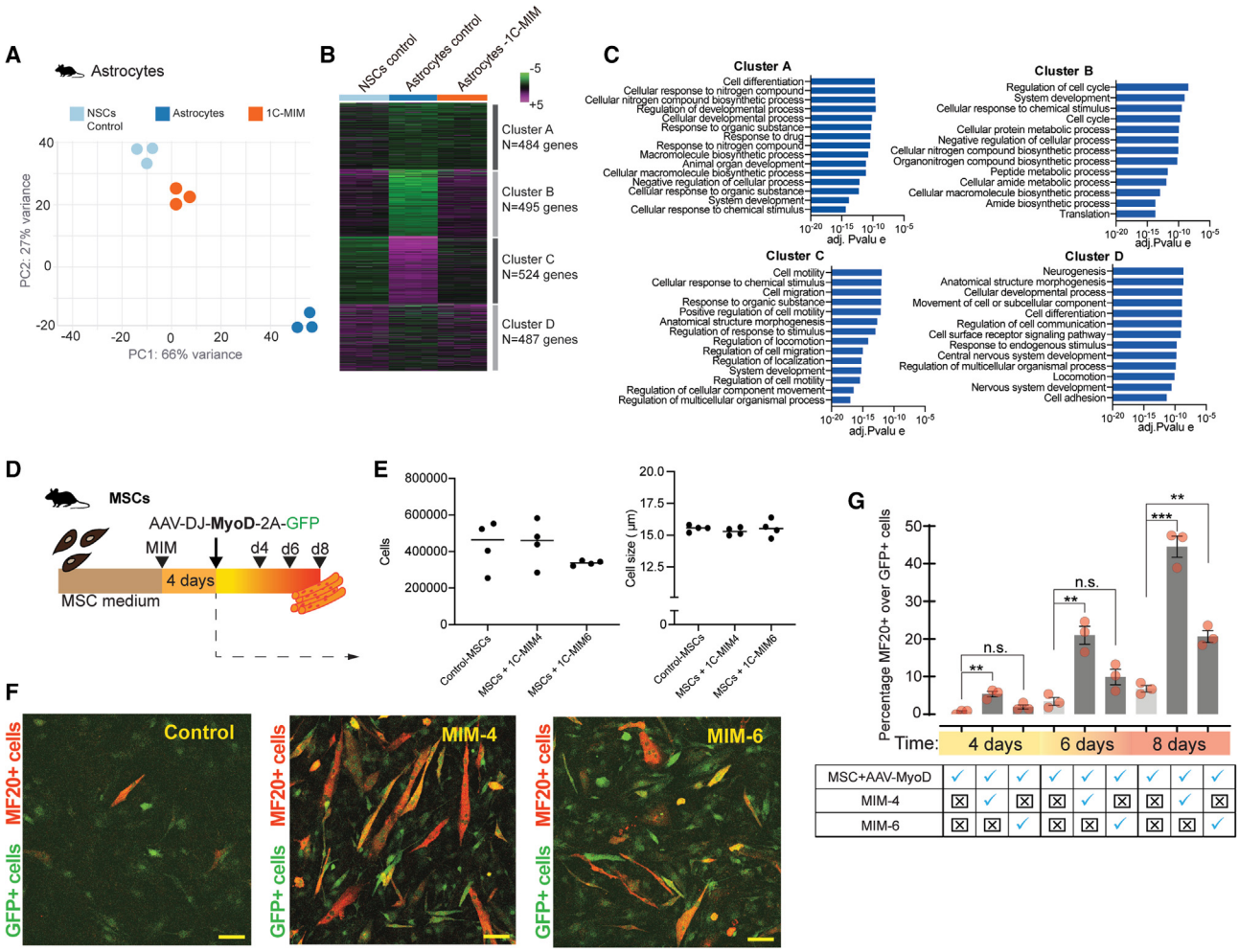

Figure 3. Biochemical transitional niche streamlines transdifferentiation events between cell types

(A–C) Transcriptional characterization of the identity acquired by astrocytes after 1C-MIM supplementation. (A) PCA map of control astrocytes, 1C-MIM-astrocytes, and NSCs based on the gene-normalized expression level. The transcriptomic profile was obtained by bulk RNA-seq; each sample is represented by single dots (n = 3). (B) HCA performed using a Euclidean distance metric comparing gene expression profiles; magenta to green color gradient indicates higher to lower expression *Z* score and K-means analysis of DEGs classified in four clusters with the indicated number of genes. (C) Gene Ontology-enriched categories in each identified cluster from (B).

(D–G) Functional assay for the conversion of MSCs into MBs accelerated by 1C-MIM. Schematic representation of the pretreatment with 1C-MIM after the infection with AAV-DJ-MyoD-2A-GFP and times for evaluation in (D). Evaluation of cell number and size of population after 4 days of 1C-MIM or control treatments in (E), where MIM-6 contains methionine, glycine, putrescine, cysteine, and S-adenosylmethionine, while MIM-4 contains the former composition minus cysteine and minus S-adenosylmethionine. (F) Representative images of transdifferentiated cells, in green the GFP expression (infected cells that harbor MyoD), and in red MF20 (transdifferentiated cells expressing antigen myosin heavy chain [MyH1E]) evaluated at day 8 post-infection. Scale bar: 50 μm. (G) Percentages of MF20+ cells over GFP expressed cells obtained by direct counting of fluorescents cells. Significant differences indicated as **p<0.005 and *** p<0.001.

Dots represent each sample, n ≥ 3, and bars the average ± SEM.

See also Figure S5.

as observed by the earlier detection of MF20+ cells on day 4, when the infection alone still did not show any converted cells (Figures 3D–3G). Interestingly, more GFP+ cells over the same number of cells were observed on day 8 post-infection, which may reflect an additional influence of the cocktail in the viral transduction, independently of the efficiency of transdifferentiation (which has been normalized to GFP). Of note, no significant differences after the 4 days of supplementation (and before transduction) were observed between control and supplemented cells (Figure 3E); particularly, on the combination of 4 metabolites, more impact in transdifferentiation was detected (Figures 3F and 3G). Also, we challenged the supplementation in an MB-independent model. We treated human fibroblasts with neurogenin (*NGN1/2*) with or without 1C-MIM and evaluated the efficiency of neuronal conversion (Figure S5F). We found that 1C-MIM caused a reduction in the fibroblast marker CD44 and increased neural marker expression (Figures S5G–S5J). Overall, the above results demonstrate that exposing cells to a

biochemical niche abundant in 1C metabolites favors the niche that facilitates traits for plasticity.

In vivo 1C-metabolite intervention accelerates muscle recovery after injury in young and old mice

Next, to validate the potential translatability of 1C-MIM, we performed an *in vivo* intervention. We chose the model of muscle degeneration by cardiotoxin (CTX), which injures muscular fibers with subsequent activation of the repair mechanism involving sequential transformative cell events.[14] We performed an *in vivo* intervention using 87 wild-type mice (see allocated groups in Figure S6A). Because this intervention consisted of a drinking supplementation, we measured the drinking volumes, observing just a slight trend of an increase in the drinking of 1C-MIM water compared to control standard water (Figure S6B). The drinking supplementation did not induce weight changes (Figure S6C). In addition, a scramble drinking control composed of six metabolites not directly related to 1C metabolism and an intervention of 3 month glycine supplementation were included (glycine, as an amino acid part of 1C and with reported effects in muscle building[15]). Neither scramble nor glycine altered the volume of drinking or weight (Figures S6B and S6C).

As part of the *in vivo* validation, we compared the motor capacity in the intervened young and old mice. As the first step, we preconditioned the mice to the open field test (by placing the mice in the area for 1 h and 2–3 times at least 1 week before inducing the injury) as the last habituation the day before CTX injection (Figure 4A). Next, we confirmed that CTX injury impaired the mice's movement, as observed by a reduction in motor responses in terms of velocity and jumps, together with an increase in resting time, measured 5 h after recovering from anesthesia (Figure S6D). Interestingly, only 24 h after injury, we observed an increase in ambulatory distance and, consequently, a decrease in the resting time in those mice supplemented with 1C-MIM (Figures 4B and 4C). Only a trend in the improvement of other parameters like the number of jumps and ambulatory time was detected: 59% and 61% of the variation of the relative number of jumps and ambulatory time accounted for the regeneration progression, while the velocity variation is not accounted for that recovery (Figure 4D). Of note, the resting time was the parameter that showed the most relevant difference between groups after CTX injury (i.e., mice rest for more time), and it was also compared to the glycine intervention and to the scramble intervention to test specificity. In summary, by comparison with the other control supplementations, a faster motor recovery was detected in mice supplemented with 1C-MIM; in second place was the group supplemented with glycine; and control-untreated and scramble-supplemented mice were behind, with no difference between them (Figure 4C). Overall, mice reduce the resting time (likewise increase ambulatory distance) as muscle regeneration (recovery) progresses.

Next, we analyzed what happened at the tissue level. Our observations corroborated the improvement seen in 1C-MIM-supplemented mice. After an injury, the recovery of muscle architecture is concurrent with the appearance of centrally nucleated regenerating fibers; thus, we wondered whether 1C-MIM benefits the appearance rate of central-nucleated fibers. We observed a 2.4-fold increase in central-nucleated fibers on day 2 in 1C-MIM-supplemented mice (i.e., meeting a number of center-nucleated fibers usually observed in controls after day 7), suggesting that the repair occurs faster in 1C-MIM animals (Figures 5A and 5B). This effect occurs despite having started from a comparable degree of damage with CTX injection (Figure S7A).

Previous studies have shown that activated satellite cells (SCs) are prominent on day 7—after CTX injury—and reduced beyond 11 days.[14] We observed that, indeed, 1C-MIM enhances this activation, as indicated by a significant increase in the levels of Pax7+ cells. These results were consistently obtained in independent treated groups, including young—male or female—and aged mice (Figures 5C and 5D). Moreover, during the regeneration process, the myofibers from 1C-MIM-supplemented mice exhibited increased cross-sectional areas compared to their untreated counterparts, indicating that this intervention accelerates recovery (Figures 5E–5G). The 1C-MIM intervention did not impact the myofiber size in control animals without injury (Figure S7B). Of note, the scramble 3 month intervention did not impact the myofiber size (Figure 5H), whereas the 3 month glycine supplementation had an effect, increasing the size as reported by others,[15] but the effect of 1C-MIM supplementation was still superior (Figure 5H).

Finally, to get mechanistic insights of 1C-MIM in muscle tissue, we measured DNA methylation age in mice quadriceps (without injury). We found that 1C-MIM muscle exhibited a discrete but significant reduction in age according to Horvath's muscle clock (Figure S7C). This suggests that rejuvenation by DNA methylation plays a minor role. Because in the earlier *in vitro* models analyzed (both myofibers and astrocytes), modulations in the cell cycle occurred after the addition of 1C-MIM, we measured the Ki67+ cells in mice muscle over the different supplementations, and only 1C-MIM—but not scramble, glycine, or control—had a significant increase in Ki67+ cells (Figure 6A). To distinguish whether 1C-MIM influences proliferating MBs or quiescent SCs, we performed coimmunostaining on isolated single myofibers using MyoD and Pax7. We found that 1C-MIM increased the number of proliferating SCs (Pax7+MyoD+) and the number of quiescent SCs (Pax7+MyoD−) by 1.96- and 1.7-fold, respectively (Figure 6B). Next, we performed RNA transcriptomics, and PCA showed a clear separation of the control muscle from the 1C-MIM-supplemented mice (Figure 6C). DEG analysis (cutoff value of log2 fold change: −0.5,+0.5 and adjusted $p < 0.01$) showed 789 genes, from which 67% were downregulated and associated with immune response and collagen formation (Figures 6D–6F). Particularly, significant downregulation of the pro-tumorigenic gene *Saa3*, the pro-dystrophy gene *Timp1*, and the glycoprotein involved in inflammation and cell death *Clu* and downregulation of metallothioneins *Mt1* and Mt2, the abrogation of which has been associated with increases in myotube size and muscle strength, were observed.[16] No significant changes were found in senescent markers (Figure S7D). Conversely, supplemented 1C-MIM muscle, particularly, showed upregulation of genes such as *Lep* (a gene known for modulating the expression of metabolic and myokine genes), *Gdf5* (an inhibitor of muscle atrophy), several cadherins, *Efcab6* (related to the recruitment of the histone deacetylase complex), and *Hdac3* (histone deacetylase that regulates

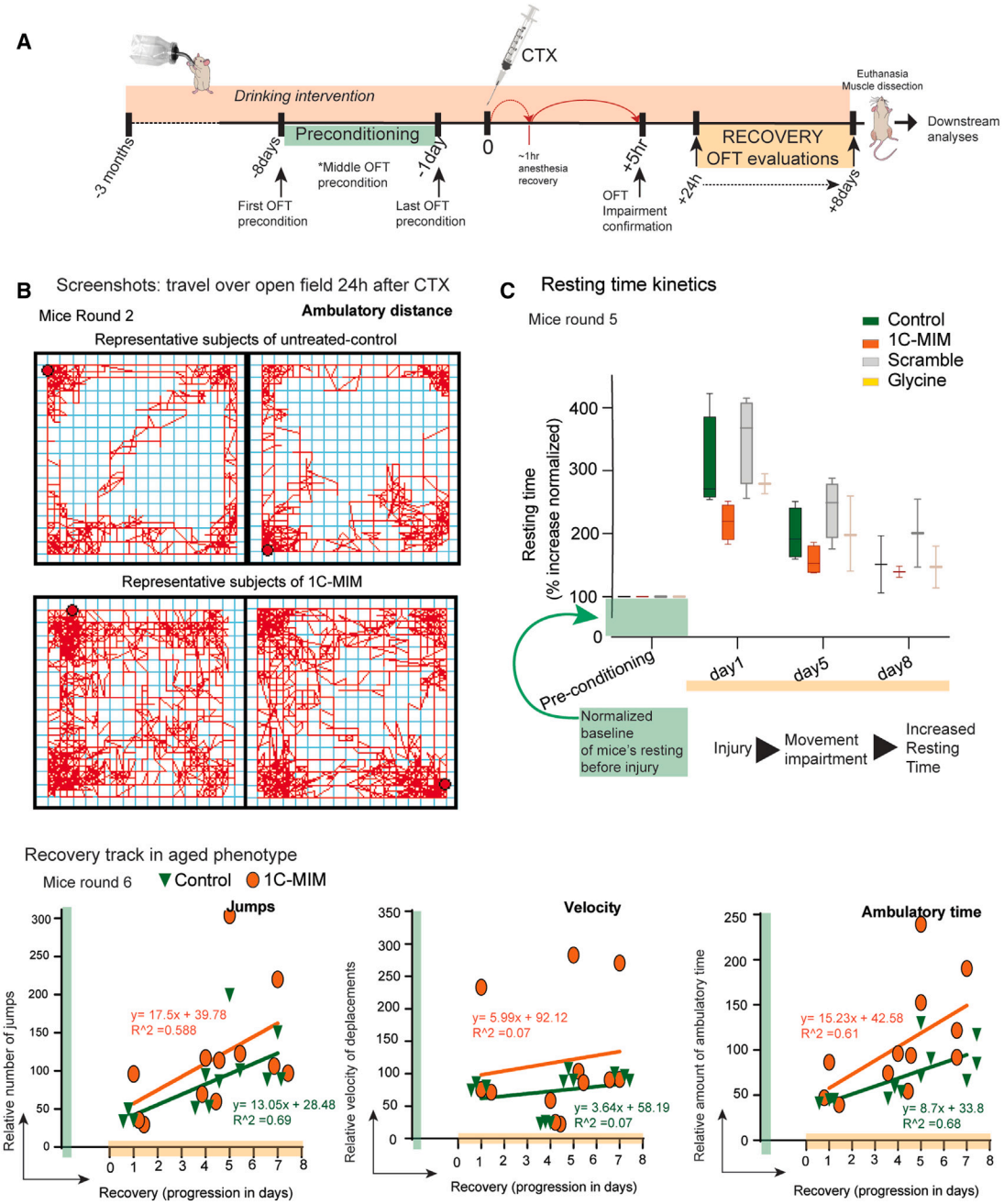

Figure 4. *In vivo* 1C-MIM intervention accelerates motor recovery from CTX injury

(A) Experimental design. The drinking intervention is maintained during all times, including 3 months before the CTX injection and 8 days of recovery after CTX. The day of CTX injection is marked in the center as "0," followed by 8 days of recovery. The green bar before CTX marks the period of behavioral preconditioning of mice to the open field test (OFT), and the orange bar after CTX marks the tracking of recovery by the OFT.

(B) Representative tracks of behavioral motor test performed in control and 1C-MIM-supplemented mice 24 h after CTX injury.

(C) Kinetics of resting, evaluated by OFT in CTX-injured mice. The resting time was recorded at 1, 5, and 8 days after cardiotoxin injury during a 60 min session. Preconditioning was performed in all animals 1 week before injury and considered as net 100% for subsequent analyses.

(D) Kinetics of jumps, velocity, and ambulatory time, evaluated by OFT in CTX-injured mice. These were recorded 1, 4 , 5 , and 7 days after cardiotoxin injury during a 60 min session. Preconditioning was performed in all animals 1 week before the injury.

Total intervention n = 87 mice. Pair comparisons at indicated groups are in Figure S6A.

See also Figures S5 and S6.

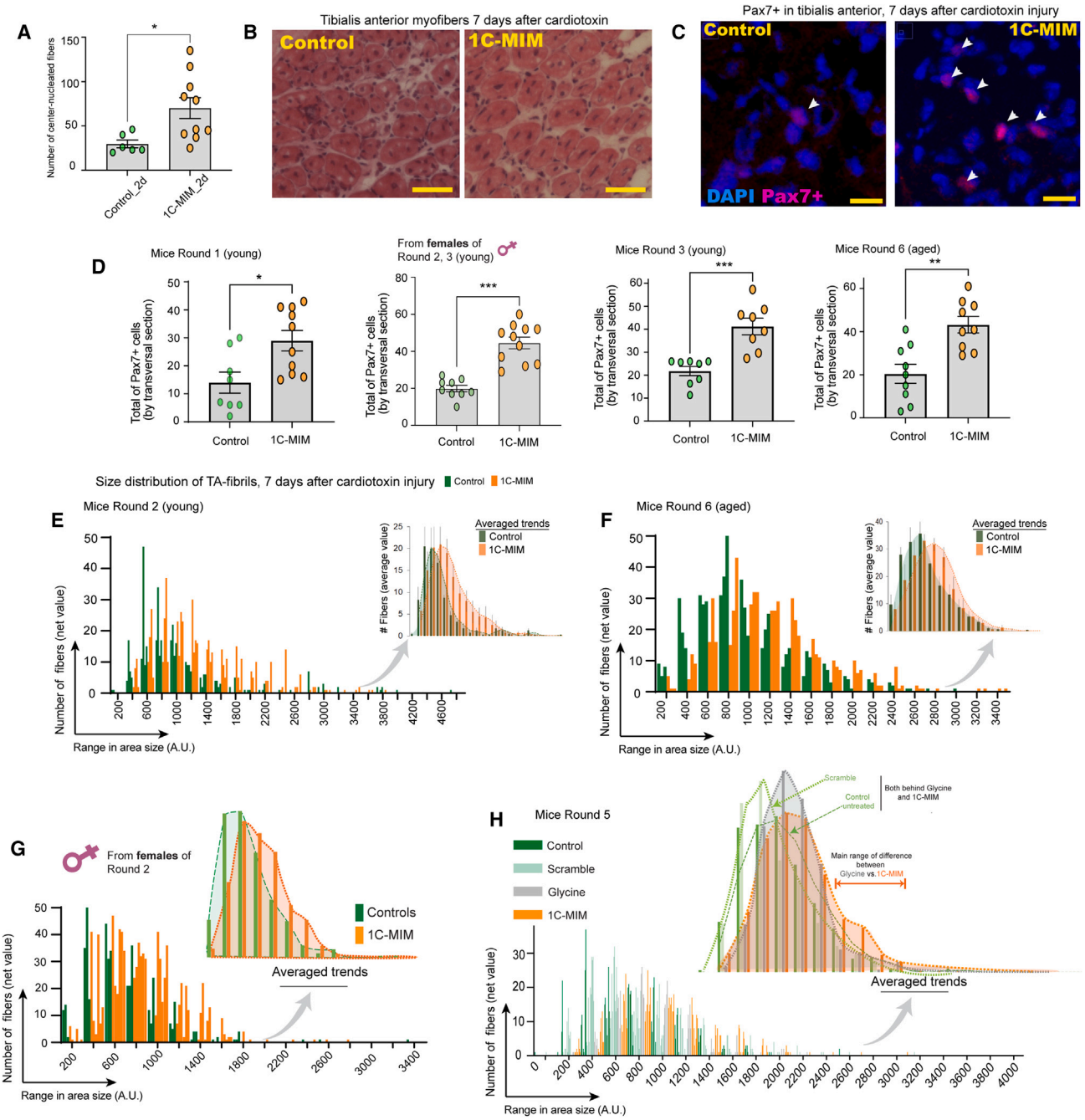

Figure 5. Muscle repair is accelerated after the intervention with 1C metabolites *in vivo*

(A) Analysis of the number of centrally nucleated cells expressed as "number of fibers/field" in control and cardiotoxin-injected muscle at day 2 in control and 1C-MIM-supplemented mice. Random fields were assessed per condition.

(B) Representative H&E staining of tibialis anterior (TA) 7 days after cardiotoxin injection in control and 1C-MIM-treated mice. Scale bar: 50 μm.

(C) Representative immunostaining of Pax7+ cells in TA 7 days after cardiotoxin injection in control and 1C-MIM-treated mice. White arrows indicate double-positive DAPI+Pax7+. Scale bar: 15 μm.

(D) Quantification of Pax7+ cells per field in the indicated group comparisons.

(E–H) Distribution of the fibers according to their size in TA muscle 7 days after cardiotoxin injection. Comparison between control vs. 1C-MIM intervention in the indicated groups. Insets on the right of each image represent averages ± SD. Note that as the curve displaces to the right, it indicates an advance in the muscle regeneration (because of the bigger size of myofibers as these recover). (H) Comparisons of the scramble supplementation of six metabolites unrelated to 1C metabolism; only glycine supplementation; the conditions control (plain water) and 1C-MIM, all were supplemented for 3 months.

Total intervention n = 87 mice. Significant differences indicated as *p<0.05, **p<0.005, and ***p<0.001. Pair comparisons at indicated groups are in Figure S6A.

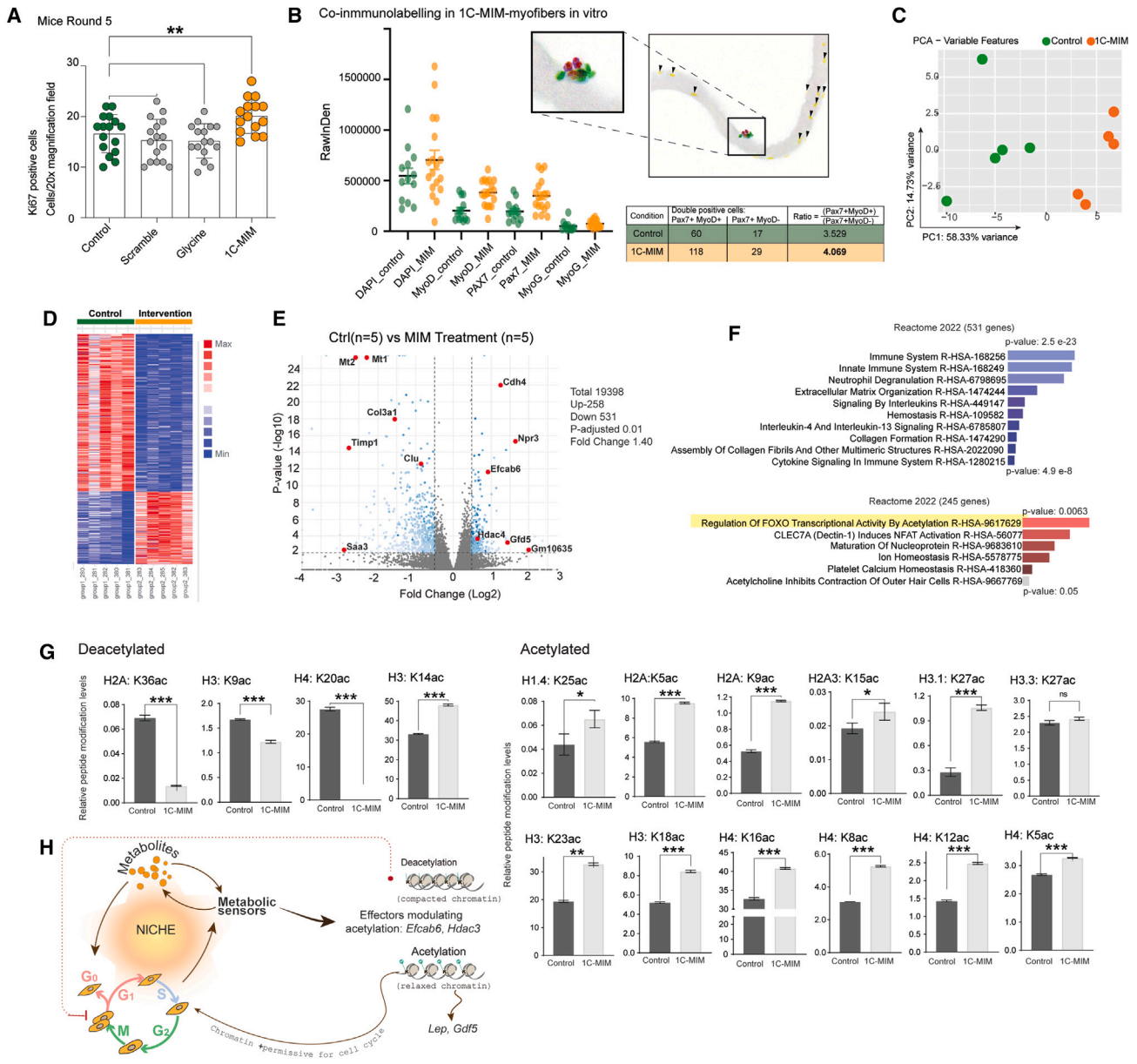

Figure 6. Modifications in acetylation and modulations on cell cycle drive the acceleration of regeneration by 1C-MIM in muscle *in vivo*

(A) Proliferation quantified by immunofluorescence and Ki67 detection.

(B) Primary myofibers were placed *in vitro* and treated with or without 1C-MIM for precise evaluation of double markers in nuclei. On the right, there is a summary table indicating the number of nuclear markers in single myofibers for control and 1C-MIM-treated double-positive and the ratio of Pax7+ vs. MyoD+ or MyoD– in myofibers exposed to the indicated conditions.

(C–F) Transcriptomic analysis of 1C-MIM quadriceps extracted from old mice after 3 months of supplementation. (C) PCA. (D) Heatmap with the total of DEGs. (E) Respective volcano plots showing DEGs as blue dots DEG, not significant genes as gray dots, and genes of interest highlighted as red dots (p-adj. <0.01). (F) Enrichment analysis of the DEGs with p-adj. < 0.01.

(G) Orthogonal readouts on the histone modifications detected by mass spectrometry on control astrocytes and 1C-MIM-supplemented astrocytes.

(H) Suggested mechanism of 1C-MIM for eliciting acceleration of the cell transition on regeneration. Several metabolic sensors respond to incoming metabolites, creating modulation feedback in the niche. Particularly, an increase in deacetylation will evoke relaxed chromatin, facilitating the expression of new genes associated with specific cell programs required for a cell in a given time (e.g., during regeneration). Thus, preloading the cells with specific metabolites may have prepared them for the rapid gene activation required for any identity transition.

Total intervention n = 87 mice. Pair comparisons at indicated groups are in Figure S6A. See also Figure S7.

Significant differences as *p<0.05, **p<0.005, and ***p<0.001.

skeletal muscle fuel metabolism). Correspondingly, gene set enrichment analysis revealed that 1C-MIM intervention was positively correlated with epigenetic regulation of gene expression, chromatin-modifying enzymes, and histone acetylation (Figure S7E). The upregulated DEG enriched for regulation of transcriptional activity by acetylation, suggesting this as the via for modulating cell cycle (Figure 6F). Orthogonal readouts obtained in astrocytes treated with 1C-MIM corroborate this regulation, as we measured the changes in the relative abundance of histone modifications induced by 1C-MIM (including acetylation, methylation, and unmarked histones). No relevant changes in methylation marks were observed, but 1C-MIM increased global acetylation marks, an event supporting the acquisition of chromatin plasticity (Figures S7E and 6G).

Overall, our results show that our 1C-MIM intervention *in vivo* accelerates the regeneration in mouse muscle, emulating the intermediate flexibility observed in the transitional state of differentiating MBs, therefore not impacting the lineage identity. Moreover, this intervention favors reprogramming transitions that enhance the myogenic potential after an injury event, thereby accelerating the recovery of a healthy state in damaged muscle.

DISCUSSION

This study shows that a biochemical intervention, mirroring physiological transitional cell states captured during *in vitro* MB differentiation, may improve tissue regeneration and function upon injury in both young and old mice. This proposition is supported by several *in vitro* (including but not limited to MB/myofibers) and *in vivo* experimental models and may take place by a discrete reprogramming process mediated by acetylation without a loss of lineage identity.

Previously, several studies have explored in-depth cell transition identities (see, for instance, Bracha et al.[4] and Peng et al.[17]). Knowledge about the biochemical demands on intermediate identity transitions is scarce. Thus, we aimed to capture the initial stages at which cells start to lose their steady state and transition to an intermediate, not-well-defined labile state that subsequently resolves in various differentiation paths within a particular lineage. In this context, through a time-dependent metabolomic approach, we identified a subset of biochemicals to formulate a supplementation we called 1C-MIM. This set of metabolites partially mimics the early-intermediate fingerprint characterized by a transient wave of metabolites belonging to the 1C network. Interestingly, we found similar metabolomic waves at the initial stages of differentiation in three multipotent models, as well as indicators of these metabolomic waves in the transient states derived from pluripotent cells. Of note, the similarities described occurred despite differences in the initial multipotent profiles, their supporting culture media, and time span differentiation disparities between cell models. This observation suggests that a 1C wave could be a potential conserved event for cells starting any identity transition. 1C metabolites may play a role in various contexts involving changes in cell identity and cell plasticity. We hypothesize that a rapid increase in 1C metabolites may prime the intracellular environment for the deactivation or activation of transcriptional networks, such as pathways that modulate the cell cycle of potential progenitors and provide substrates that enable specific epigenetic modulations,[18–20] thus favoring a state in which cells are prone to make a fate decision. Indeed, supplying 1C-associated metabolites to fully differentiated cells, both *in vivo* and *in vitro*, resulted in the acquisition of some traits of a progenitor-like state.

The loss of some mature markers without the loss of lineage identity observed after 1C-MIM supplementation and the higher responsiveness to differentiation signals resemble cell dynamic attributes previously reported in cells undergoing partial reprogramming with conventional Yamanaka factors.[21–25] This partially reprogrammed cell state has been defined as an intermediate transitional state where cells are able to retain their lineage identity, and at the same time, they are highly responsive to specific differentiation factors.[26] In our experimental designs, we could define whether the 1C-MIM effects were because of selection for remaining undifferentiated cells or reversion in the identity of myotubes. This could be assessed by looking at single isolated myofibers from mouse muscle, treated by the 1C cocktail and processed by immunocytochemistry (Figure 6B). Under these conditions, 1C-MIM myotubes showed the acquisition of some nuclei positive for Pax7 (both with and without MyoD). Since this experiment was performed with single myotubes isolated and subprocessed in low density, it is thus possible to propose the partial reversion of their identity. While this does not occur homogeneously in all myotubes, this validates the multinuclear persistence of myotubes, with some nuclei acquiring the Pax7 signal. As a disclaimer, the same validation is difficult to confirm in C2C12 cultures; this is due to the nature of the differentiation of that artificial model, where some progenitor cells may remain. Nonetheless, the observations from *in-vivo*-isolated myofibers are enough to support a partial reversion. On the other side, intriguing transcriptomic similarities were observed between astrocytes treated with 1C-MIM and the reported intermediate reprogrammed state for astrocytes.[11] We also observed that, in a transdifferentiation paradigm, cells are more receptive to changing their identity after 1C-MIM supplementation, as observed over the classic transcription factor-induced reprogramming, such as the generation of myofibers after transduction with *MyoD*.[27,28] While future expert testing *in vivo* is needed for challenging tissues like the brain, we consider the coincidences between the supplementation of 1C-MIM and pioneer observations from our lab (and others) about partial-reprogramming promoting muscle repair to be exciting.[24,25,29]

Addressing muscle regeneration using metabolites as a therapeutic approach has been extensively addressed; nonetheless, the explanations about the positive outcomes are still limited and usually consider either amino acids as merely building blocks or point to some elusive antioxidant effects.[15,30,31] Our finding about the upsurge of 1C-related biochemicals during the initiation of change of identity in normal differentiation, which boosts an environment prone to starting a cell cycle mediated by acetylation regulation, may explain the underlying process behind the positive effects observed by others in muscle supplemented particularly with amino acids like glycine or methionine. This opens a different perspective to designing more efficient interventions. Here, our results suggest that a 1C biochemical intervention is sufficient to partially elevate the plasticity of the epigenetic status. The fast capacity of metabolites for changing

the niche of cells potentially relies upon several metabolic sensors, which may represent the link to our biochemical intervention; therefore, the regulation of relevant modulators' acetylation like Hdac3, Hdac4, and Efcab6 in skeletal muscle (Figure 6E) may prime the environment for the deactivation/activation of transcriptional networks, thus favoring a state in which cells are prone to make a fate decision, facilitating the transitions needed during a regeneration process.[18–20]

While here, the 1C-MIM intervention was optimized for muscle cells (and to a lesser degree for astrocytes in culture), we emphasize the necessity of tailoring doses and type 1C metabolites further to the cell type. Only a few relevant markers of progenitor and differentiated states from several cell types were selected to observe the likelihood of having similar outcomes as those observed over myofibers (Figure S4). Larger screenings in expression markers should be done before achieving conclusions about the 1C-MIM effects in other cell types. The induction of an artificial elevation of metabolites with 1C-MIM in muscle cells can be attributed specifically to the metabolite mix 1C-MIM because a scramble metabolite combination did not reproduce the same outcome either *in vitro* or *in vivo*, providing robustness for the intervention in muscle lineage without disregarding the need of optimization for other tissues/cell types. For example, we observed that the addition of SAM or cysteine into neuronal cultures evoked cell death; thus, for testing in neurons, we removed both metabolites from the cocktail (Figure S4D). Moreover, the effects of the same cocktail in the different cell types tested in this study may also reflect the proper nature of the starting somatic population. For example, the treatment of *bona fide* sorted astrocytes with 1C-MIM may not exclude the additional plasticity of glial cells compared to myofibers *in vitro*.[32] Conversely, we tentatively assume that, regarding the metabolomic dynamics of the 1C wave found in early differentiation in MBs/myofibers, NSC/astrocytes, and MSC/chondrocytes (Figure 1), future studies may corroborate our findings and extend the commonality to more cell types. Last, but not the less, other metabolomic patterns could be explored in the future, like the U-shape that mostly reflects the biochemicals reduced during the early intermediate transition, which seems to be cell-type specific. While several details concerning how the application of 1C-MIM regulates other cell types remain to be elucidated, our observations already point to this group of effectors as targets that may lead to the development of approaches toward priming cell plasticity and reprogramming cell fate. Since chemical inductions usually offer tighter control in a stepwise modality than the direct overexpression of genes,[8,33–36] an intervention leveraging endogenous transitional cell niches may provide a powerful and clinically translatable strategy for redirecting phenotypes and restoring cell and tissue function during disease and aging.

Limitations of the study

This study took metabolomics dynamics of three cell types *in vitro* to obtain the signature during early transitions in their normal change of phenotype, and we proposed that the finding of the 1C network observed in those could be more general and that more metabolomics studies in other cell types should be done to validate that proposition. Metabolomics studies provide a snapshot of molecules, but it is important to consider that fast degradation and subtle changes in collection protocols can impact several molecules, therefore limiting the recognition of metabolites that may also have an early role in cell transitions and that are not pointed out in the current study. Finally, the use of the 1C-MIM cocktail *in vivo* requires further concentration standardization if it is aimed to be applied over other tissues than muscle and other species than mice.

STAR★METHODS

Detailed methods are provided in the online version of this paper and include the following:

- KEY RESOURCES TABLE
- RESOURCE AND AVAILABILITY
  - Lead contact
  - Materials availability
  - Data and code availability
- METHOD DETAILS
  - Animals
  - *In vitro* cell lines and primary cultures
  - Metabolome analysis
  - Concentration tests of components of one-carbon-metabolite induction medium (1C-MIM)
  - Immunocytochemistry
  - Relative measurement of methionine and S-adenosyl-methionine
  - RNA isolation and gene expression analysis by RT-PCR
  - Transdifferentiation experiments with 1C-MIM treatment
  - *In vivo* intervention
  - Muscle injury by cardiotoxin
  - Open field tests
  - Immunostaining and HE-staining
  - Myofibers area measurement
  - Single myofiber isolation
  - DNA-methylation clock from quadriceps
  - RNA-sequencing from quadriceps
  - RNA-sequencing from *in vitro* cells
  - Re-analysis of *in vitro* canonical partial reprogrammed astrocytes
  - Quantification of histone modifications
- QUANTIFICATION AND STATISTICAL ANALYSIS

SUPPLEMENTAL INFORMATION

Supplemental information can be found online at https://doi.org/10.1016/j.xcrm.2024.101449.

ACKNOWLEDGMENTS

We thank Ruben Rabadan-Ros, Javier Prieto, Paloma Martinez-Redondo, and Nicola Allen for helpful discussions; David O'Keefe and Mallory Shields for manuscript editing; Saskia Linder, Amy Nemeth, Jingkai Wang, Paola Moreno, Mariana Morales, and Audrey Kristin for technical assistance; May Schwarz and Peter Schwarz for administrative assistance; Dr. Zhiqiu Man for providing human astrocyte cultures; and Dr. Hitoshi Niwa for providing the ZHBTcH4 ESCs. Special thanks to Greg Palczewski for his valuable help in

metabolomics. Thanks to Nasun Han and Rachel Feiring for supporting genomics and cell culture work, respectively, at Altos Labs. Work in the laboratories of J.Q. and G.-H.L. was supported by the National Natural Science Foundation of China (82125011 and 81921006), the National Key Research and Development Program of China (2020YFA0804000 and 2022YFA1103700), and the CAS Project for Young Scientists in Basic Research (YSBR-076). This work was partially supported by King Abdullah University of Science and Technology (OSR-2015-CRG4-2631), Universidad Católica San Antonio de Murcia, Inventium, and Fundación Dr. Pedro Guillen.

AUTHOR CONTRIBUTIONS

Conceptualization, R.H.-B., P.M., and J.C.I.B.; methodology, R.H.-B., E.A.M., C.Z., R.D.S., C.W., V.L., S.M., E.N.D., C.R.E., T.H., H.-K.L., and I.G. (for general research and development), S.S. and C.W. (for transdifferentiation experiments), Y.S. (on human fibroblast cultures), V.L. and A.A.-V. (histochemical evaluations), and F.H., M.Y., I.G., C.W., and R.H.-B. (*in vivo* experiments); formal analysis, L.S. and Y.O. (transcriptomic analyses), R.H.-B. and Y.O. (metabolome analysis), R.H.-B., C.F., S.M., A.A.-V., and H.-K.L. (gene expression analysis), and S.H. (DNA methylation for Clock-mDNAge analyses); data interpretation, A.A.-V., T.H., M.Y., H.-K.L., E.N.D., P.G., C.R.E., P.R., J.Q., C.Z., and G.-H.L.; visualization and writing, R.H.-B., J.C.I.B., and P.M. (with the input of all other authors).

DECLARATION OF INTERESTS

Patent applications have been filed related to the subject matter of this publication. R.H.-B., C.W., C.Z., S.M., F.H., V.L., I.G., S.S., M.Y., Y.S., A.A.-V., C.R.E., P.R., S.H., and J.C.I.B. are employees of Altos Labs.

Received: May 24, 2022
Revised: October 10, 2023
Accepted: February 8, 2024
Published: March 19, 2024

REFERENCES

1. Moran, J.L., Li, Y., Hill, A.A., Mounts, W.M., and Miller, C.P. (2002). Gene expression changes during mouse skeletal myoblast differentiation revealed by transcriptional profiling. Physiol. Genomics *10*, 103–111. https://doi.org/10.1152/physiolgenomics.00011.2002.
2. Riuzzi, F., Sorci, G., Sagheddu, R., and Donato, R. (2012). HMGB1-RAGE regulates muscle satellite cell homeostasis through p38-MAPK- and myogenin-dependent repression of Pax7 transcription. J. Cell Sci. *125*, 1440–1454. https://doi.org/10.1242/jcs.092163.
3. Furusawa, C., and Kaneko, K. (2012). A Dynamical-Systems View of Stem Cell Biology. Science *338*, 215–217. https://doi.org/10.1126/science.1224311.
4. Bracha, A.L., Ramanathan, A., Huang, S., Ingber, D.E., and Schreiber, S.L. (2010). Carbon metabolism-mediated myogenic differentiation. Nat. Chem. Biol. *6*, 202–204. https://doi.org/10.1038/nchembio.301.
5. Magistretti, P.J., and Allaman, I. (2018). Lactate in the brain: from metabolic end-product to signalling molecule. Nat. Rev. Neurosci. *19*, 235–249. https://doi.org/10.1038/nrn.2018.19.
6. Niwa, H., Miyazaki, J., and Smith, A.G. (2000). Quantitative expression of Oct-3/4 defines differentiation, dedifferentiation or self-renewal of ES cells. Nat. Genet. *24*, 372–376. https://doi.org/10.1038/74199.
7. Chen, J., Liu, J., Chen, Y., Yang, J., Chen, J., Liu, H., Zhao, X., Mo, K., Song, H., Guo, L., et al. (2011). Rational optimization of reprogramming culture conditions for the generation of induced pluripotent stem cells with ultra-high efficiency and fast kinetics. Cell Res. *21*, 884–894. https://doi.org/10.1038/cr.2011.51.
8. Li, X., Xu, J., and Deng, H. (2018). Small molecule-induced cellular fate reprogramming: promising road leading to Rome. Curr. Opin. Genet. Dev. *52*, 29–35. https://doi.org/10.1016/j.gde.2018.05.004.
9. Lei, H., Leong, D., Smith, L.R., and Barton, E.R. (2013). Matrix metalloproteinase 13 is a new contributor to skeletal muscle regeneration and critical for myoblast migration. Am. J. Physiol. Cell Physiol. *305*, C529–C538. https://doi.org/10.1152/ajpcell.00051.2013.
10. Filvaroff, E.H., Guillet, S., Zlot, C., Bao, M., Ingle, G., Steinmetz, H., Hoeffel, J., Bunting, S., Ross, J., Carano, R.A.D., et al. (2002). Stanniocalcin 1 Alters Muscle and Bone Structure and Function in Transgenic Mice. Endocrinology *143*, 3681–3690. https://doi.org/10.1210/en.2001-211424.
11. Nakajima-Koyama, M., Lee, J., Ohta, S., Yamamoto, T., and Nishida, E. (2015). Induction of Pluripotency in Astrocytes through a Neural Stem Cell-like State. J. Biol. Chem. *290*, 31173–31188. https://doi.org/10.1074/jbc.M115.683466.
12. Liu, L., Michowski, W., Kolodziejczyk, A., and Sicinski, P. (2019). The cell cycle in stem cell proliferation, pluripotency and differentiation. Nat. Cell Biol. *21*, 1060–1067. https://doi.org/10.1038/s41556-019-0384-4.
13. Wu, J., Ocampo, A., and Belmonte, J.C.I. (2016). Cellular Metabolism and Induced Pluripotency. Cell *166*, 1371–1385. https://doi.org/10.1016/j.cell.2016.08.008.
14. Ramadasan-Nair, R., Gayathri, N., Mishra, S., Sunitha, B., Mythri, R.B., Nalini, A., Subbannayya, Y., Harsha, H.C., Kolthur-Seetharam, U., and Srinivas Bharath, M.M. (2014). Mitochondrial alterations and oxidative stress in an acute transient mouse model of muscle degeneration: implications for muscular dystrophy and related muscle pathologies. J. Biol. Chem. *289*, 485–509. https://doi.org/10.1074/jbc.M113.493270.
15. Lin, C., Han, G., Ning, H., Song, J., Ran, N., Yi, X., Seow, Y., and Yin, H. (2020). Glycine Enhances Satellite Cell Proliferation, Cell Transplantation, and Oligonucleotide Efficacy in Dystrophic Muscle. Mol. Ther. *28*, 1339–1358. https://doi.org/10.1016/j.ymthe.2020.03.003.
16. Summermatter, S., Bouzan, A., Pierrel, E., Melly, S., Stauffer, D., Gutzwiller, S., Nolin, E., Dornelas, C., Fryer, C., Leighton-Davies, J., et al. (2017). Blockade of Metallothioneins 1 and 2 Increases Skeletal Muscle Mass and Strength. Mol. Cell Biol. *37*, e00305-16. https://doi.org/10.1128/MCB.00305-16.
17. Peng, M., Yin, N., Chhangawala, S., Xu, K., Leslie, C.S., and Li, M.O. (2016). Aerobic glycolysis promotes T helper 1 cell differentiation through an epigenetic mechanism. Science *354*, 481–484. https://doi.org/10.1126/science.aaf6284.
18. Carey, B.W., Finley, L.W.S., Cross, J.R., Allis, C.D., and Thompson, C.B. (2015). Intracellular α-ketoglutarate maintains the pluripotency of embryonic stem cells. Nature *518*, 413–416. https://doi.org/10.1038/nature13981.
19. Ryall, J.G., Cliff, T., Dalton, S., and Sartorelli, V. (2015). Metabolic Reprogramming of Stem Cell Epigenetics. Cell Stem Cell *17*, 651–662. https://doi.org/10.1016/j.stem.2015.11.012.
20. Wellen, K.E., Hatzivassiliou, G., Sachdeva, U.M., Bui, T.V., Cross, J.R., and Thompson, C.B. (2009). ATP-citrate lyase links cellular metabolism to histone acetylation. Science *324*, 1076–1080. https://doi.org/10.1126/science.1164097.
21. Browder, K.C., Reddy, P., Yamamoto, M., Haghani, A., Guillen, I.G., Sahu, S., Wang, C., Luque, Y., Prieto, J., Shi, L., et al. (2022). In vivo partial reprogramming alters age-associated molecular changes during physiological aging in mice. Nat. Aging *2*, 243–253. https://doi.org/10.1038/s43587-022-00183-2.
22. Hishida, T., Yamamoto, M., Hishida-Nozaki, Y., Shao, C., Huang, L., Wang, C., Shojima, K., Xue, Y., Hang, Y., Shokhirev, M., et al. (2022). In vivo partial cellular reprogramming enhances liver plasticity and regeneration. Cell Rep. *39*, 110730. https://doi.org/10.1016/j.celrep.2022.110730.
23. Gill, D., Parry, A., Santos, F., Okkenhaug, H., Todd, C.D., Hernando-Herraez, I., Stubbs, T.M., Milagre, I., and Reik, W. (2022). Multi-omic rejuvenation of human cells by maturation phase transient reprogramming. Elife *11*, e71624. https://doi.org/10.7554/eLife.71624.
24. Ocampo, A., Reddy, P., Martinez-Redondo, P., Platero-Luengo, A., Hatanaka, F., Hishida, T., Li, M., Lam, D., Kurita, M., Beyret, E., et al. (2016).

In Vivo Amelioration of Age-Associated Hallmarks by Partial Reprogramming. Cell *167*, 1719–1733.e12. https://doi.org/10.1016/j.cell.2016.11.052.

25. Wang, C., Rabadan Ros, R., Martinez-Redondo, P., Ma, Z., Shi, L., Xue, Y., Guillen-Guillen, I., Huang, L., Hishida, T., Liao, H.-K., et al. (2021). In vivo partial reprogramming of myofibers promotes muscle regeneration by remodeling the stem cell niche. Nat. Commun. *12*, 3094. https://doi.org/10.1038/s41467-021-23353-z.
26. Lehmann, M., Canatelli-Mallat, M., Chiavellini, P., Cónsole, G.M., Gallardo, M.D., and Goya, R.G. (2019). Partial Reprogramming As An Emerging Strategy for Safe Induced Cell Generation and Rejuvenation. Curr. Gene Ther. *19*, 248–254. https://doi.org/10.2174/1566523219666190902154511.
27. Xu, B., Siehr, A., and Shen, W. (2020). Functional skeletal muscle constructs from transdifferentiated human fibroblasts. Sci. Rep. *10*, 22047. https://doi.org/10.1038/s41598-020-78987-8.
28. Yagi, M., Ji, F., Charlton, J., Cristea, S., Messemer, K., Horwitz, N., Di Stefano, B., Tsopoulidis, N., Hoetker, M.S., Huebner, A.J., et al. (2021). Dissecting dual roles of MyoD during lineage conversion to mature myocytes and myogenic stem cells. Genes Dev. *35*, 1209–1228. https://doi.org/10.1101/gad.348678.121.
29. Sarkar, T.J., Quarta, M., Mukherjee, S., Colville, A., Paine, P., Doan, L., Tran, C.M., Chu, C.R., Horvath, S., Qi, L.S., et al. (2020). Transient non-integrative expression of nuclear reprogramming factors promotes multifaceted amelioration of aging in human cells. Nat. Commun. *11*, 1545. https://doi.org/10.1038/s41467-020-15174-3.
30. Love, A., Cotter, M.A., and Cameron, N.E. (1996). Nerve function and regeneration in diabetic and galactosaemic rats: antioxidant and metal chelator effects. Eur. J. Pharmacol. *314*, 33–39. https://doi.org/10.1016/S0014-2999(96)00528-6.
31. Wu, C.-T., Liao, J.-M., Ko, J.-L., Lee, Y.-L., Chang, H.-Y., Wu, C.-H., and Ou, C.-C. (2019). D-Methionine Ameliorates Cisplatin-Induced Muscle Atrophy via Inhibition of Muscle Degradation Pathway. Integr. Cancer Ther. *18*, 1534735419828832. https://doi.org/10.1177/1534735419828832.
32. Fu, Y., Yang, M., Yu, H., Wang, Y., Wu, X., Yong, J., Mao, Y., Cui, Y., Fan, X., Wen, L., et al. (2021). Heterogeneity of glial progenitor cells during the neurogenesis-to-gliogenesis switch in the developing human cerebral cortex. Cell Rep. *34*, 108788. https://doi.org/10.1016/j.celrep.2021.108788.
33. Beyret, E., Martinez Redondo, P., Platero Luengo, A., and Izpisua Belmonte, J.C. (2018). Elixir of Life: Thwarting Aging With Regenerative Reprogramming. Circ. Res. *122*, 128–141. https://doi.org/10.1161/CIRCRESAHA.117.311866.
34. Kim, Y., Jeong, J., and Choi, D. (2020). Small-molecule-mediated reprogramming: a silver lining for regenerative medicine. Exp. Mol. Med. *52*, 213–226. https://doi.org/10.1038/s12276-020-0383-3.
35. Liu, Y., Song, Z., Zhao, Y., Qin, H., Cai, J., Zhang, H., Yu, T., Jiang, S., Wang, G., Ding, M., and Deng, H. (2006). A novel chemical-defined medium with bFGF and N2B27 supplements supports undifferentiated growth in human embryonic stem cells. Biochem. Biophys. Res. Commun. *346*, 131–139. https://doi.org/10.1016/j.bbrc.2006.05.086.
36. Shi, Y., Hou, L., Tang, F., Jiang, W., Wang, P., Ding, M., and Deng, H. (2005). Inducing Embryonic Stem Cells to Differentiate into Pancreatic β Cells by a Novel Three-Step Approach with Activin A and All- *Trans* Retinoic Acid. STEM CELLS *23*, 656–662. https://doi.org/10.1634/stemcells.2004-0241.
37. Xia, J., Psychogios, N., Young, N., and Wishart, D.S. (2009). MetaboAnalyst: a web server for metabolomic data analysis and interpretation. Nucleic Acids Research *37*, W652–W660. https://doi.org/10.1093/nar/gkp356.
38. Heberle, H., Meirelles, G.V., Da Silva, F.R., Telles, G.P., and Minghim, R. (2015). InteractiVenn: a web-based tool for the analysis of sets through Venn diagrams. BMC Bioinformatics *16*, 169. https://doi.org/10.1186/s12859-015-0611-3.
39. Chen, E.Y., Tan, C.M., Kou, Y., Duan, Q., Wang, Z., Meirelles, G.V., Clark, N.R., and Ma'ayan, A. (2013). Enrichr: interactive and collaborative HTML5 gene list enrichment analysis tool. BMC Bioinformatics *14*, 128. https://doi.org/10.1186/1471-2105-14-128.
40. Raudvere, U., Kolberg, L., Kuzmin, I., Arak, T., Adler, P., Peterson, H., and Vilo, J. (2019). g:Profiler: a web server for functional enrichment analysis and conversions of gene lists (2019 update). Nucleic Acids Research *47*, W191–W198. https://doi.org/10.1093/nar/gkz369.
41. Mauri, M., Elli, T., Caviglia, G., Uboldi, G., and Azzi, M. (2017). RAWGraphs: A Visualisation Platform to Create Open Outputs. In Proceedings of the 12th Biannual Conference on Italian SIGCHI Chapter (ACM), pp. 1–5. https://doi.org/10.1145/3125571.3125585.
42. Subramanian, A., Tamayo, P., Mootha, V.K., Mukherjee, S., Ebert, B.L., Gillette, M.A., Paulovich, A., Pomeroy, S.L., Golub, T.R., Lander, E.S., et al. (2005). Gene set enrichment analysis: A knowledge-based approach for interpreting genome-wide expression profiles. Proc. Natl. Acad. Sci. USA *102*, 15545–15550. https://doi.org/10.1073/pnas.0506580102.
43. Mozhui, K., Lu, A.T., Li, C.Z., Haghani, A., Sandoval-Sierra, J.V., Wu, Y., Williams, R.W., and Horvath, S. (2022). Genetic loci and metabolic states associated with murine epigenetic aging. Elife *11*, e75244. https://doi.org/10.7554/eLife.75244.

STAR★METHODS

KEY RESOURCES TABLE

REAGENT or RESOURCE	SOURCE	IDENTIFIER
Antibodies		
anti-Nestin	Millipore	Cat# MAB353, RRID:AB_94911
anti-Pax7	DSHB	Cat# AB_528428, RRID:AB_528428
anti-MF20	DSHB	Cat# AB_2147781, RRID:AB_2147781
anti-MyoD	Santa Cruz	Cat# sc-377460, RRID:AB_2813894
anti-Ki67	Cell Signaling	Cat# 12202, RRID:AB_2620142
Donkey anti-Rabbit IgG (H + L) Highly Cross-Adsorbed Secondary Antibody, Alexa Fluor 568	Thermo Fisher Scientific	Cat# A10042, RRID:AB_2534017
Goat anti-Mouse IgG2a Cross-Adsorbed Secondary Antibody, Alexa Fluor 568	Thermo Fisher Scientific	Cat# A21134, RRID:AB_2535773
Donkey anti-Rabbit IgG (H + L) Highly Cross-Adsorbed Secondary Antibody, Alexa Fluor 488	Thermo Fisher Scientific	Cat# A21206, RRID:AB_2535792
Goat anti-Chicken IgY (H + L) Secondary Antibody, Alexa Fluor 488	Thermo Fisher Scientific	Cat# A11039, RRID:AB_2534096
H3K27me3 antibody	Active Motif	Cat# 39155, RRID:AB_2561020
Chemicals, peptides, and recombinant proteins		
rhEFG	Thermo Fisher Scientific	Cat# PH G0311
Fetal Bovine Serum	Thermo Fisher Scientific	Cat# 16000-044
Maxima H Minus cDNA Synthesis Master MIX	Thermo Fisher Scientific	Cat# M1662
Lipofectamine 2000	Thermo Fisher Scientific	Cat# 11668019
SB 431542	Tocris	Cat# 1614
SsoAdvanced Universal SYBR *Green Supermix	BIORAD	Cat# 1725274
Astrocyte Growth Supplement	ScienCell	Cat# 1852
L-Methionine	Sigma	Cat# M5308
L-Threonine	Sigma	Cat# T8441
Glycine	Sigma	Cat# G5417
Putrescine dihydrochloride	Sigma	Cat# P5780
L-cysteine	Sigma	Cat# C7477
S-adenosylmethionine tosylate	Cayman Chemical	Cat# 16376
L-Arginine	Sigma	Cat# A8094
Creatine	Sigma	Cat# C0780
D-Fructose	Sigma	Cat# F0127
L-Histidine	Sigma	Cat# H5659
L-Leucine	Sigma	Cat# L8912
L-Valine	Sigma	Cat# V0513
Taurine	Sigma	Cat# T8691
r-bFGF	Joint Protein Central	Cat# BBI-EXP-002
Y27632	Reagents Direct	Cat# 53-B85-50
LDN193189	MILTENYI BIOTEC	Cat# 130-106-540
cAMP	Cayman Chemical	Cat# 18820
CHIR99021	Selleck	Cat# S2924
IWP4	Stemgent	Cat# 04-0036

(*Continued on next page*)

Continued

REAGENT or RESOURCE	SOURCE	IDENTIFIER
B-27 Supplement	Life Technologies	Cat# 17504-044
N2 Supplement	Life Technologies	Cat# 17502048
Cardiotoxin	Latoxan S.A.S.	Cat# L8102
AAV-MyoD-2A-GFP	VectorBiolabs	Cat#230116
Critical commercial assays		
STEMPro Chondrogenesis Differentiation Kit	Thermo Fisher Scientific	Cat# A10069
RNeasy Plus Mini kit	QIAGEN	Cat# 74106
Anti-GLAST (ACSA-1) Microbead Kit	MILTENYI BIOTEC	Cat# 130-095-825
Magnetic plate	OZ Biosciences	Cat# MF10000
Combimag	OZ Biosciences	Cat# CM20200
Methionine Assay Kit (Fluorometric)	ABCAM	Cat# ab234041
S-Adenosylmethionine (SAM) ELISA Kit	Cell Biolabs	Cat# STA-672
Experimental models: Cell lines		
Mouse Adipose-Derived Mesenchymal Stem Cells OriCell Strain	Cyagen	Cat# C57BL/6
Myoblasts C2C12	ATCC	Cat# CRL 1772
Mouse embryonic stem cells: ZHBTcH4 ESCs	Laboratory of Dr. Hitoshi Niwa	Laboratory of Dr. Hitoshi Niwa
Human BJ-fibroblasts	ATCC	Cat# CRL-2522
Human ESC H1	WiCell	Cat#WA01
Experimental models: Organisms/strains		
Mouse ICR (CD-1®) outbred mice	Envigo	Cat# Hsd:ICR (CD-1®)
Mouse C57BL inbred mice	Jackson	JAX® Mice
Oligonucleotides		
See Table S5 for list of primers	Eton Bioscience	
Software and algorithms		
ImageJ	Open Source	https://imagej.nih.gov/ij/
Metabolon Portal ®	Metabolon®	https://portal.metabolon.com/en/login
Metaboanalyst	Xia et al., 2009[37]	https://www.metaboanalyst.ca/
ArrayStudio	Omicsoft	http://omicsoft.com/software/ArrayStudioLauncher/publish.htm
Basepair	Basepair	https://www.basepairtech.com/
Interactivenn	Heberle et al., 2015[38]	http://www.interactivenn.net/
Enrichr	Chen et al., 2013[39]	https://maayanlab.cloud/Enrichr/
gProfiler	Raudvere et al., 2019[40]	https://biit.cs.ut.ee/gprofiler/gost
Graph Pad Prism8	© 2018 GraphPad Software	https://www.graphpad.com/scientific-software/prism/
Raw graphs software	Mauri et al., 2017[41]	https://rawgraphs.io/
Adobe Illustrator	© 2020 Adobe	https://www.adobe.com/
ToppGene Suite	Cincinnati Children's Hospital Medical Center	https://toppgene.cchmc.org/
Gene Set Enrichment Analysis (GSEA) software	Subramanian et al., 2005[42]	https://www.gsea-msigdb.org/gsea/index.jsp
Activity Monitor Software	Med Associates Inc.	https://med-associates.com/product/activity-monitor-7-software/
Deposited Data		
Metabolomics	Mendeley	Mendeley Data:https://doi.org/10.17632/ghjgddwfzz.1
RPC strategy	Mendeley	Mendeley Data: https://doi.org/10.17632/zgftdrtrxx.1
Transcriptomics: Myoblast differentiation and Neural stem cell transitions	Gene Expression Omnibus	Database GEO: GSE155193 and GSE145897

(*Continued on next page*)

Continued

REAGENT or RESOURCE	SOURCE	IDENTIFIER
Transcriptomics: Effect of metabolite intervention in mice muscle gene expression	Gene Expression Omnibus	Database GEO: GSE229533
Transcriptomics: Effect of metabolites supplementation on C2C12 gene expression	Gene Expression Omnibus	Database GEO: GSE229534

RESOURCE AND AVAILABILITY

Lead contact

Further information and requests for resources and reagents should be directed and will be fulfilled by the lead contact Juan Carlos Belmonte (jcbelmonte@altoslabs.com).

Materials availability

This study did not generate unique reagents. A patent application has been filed related to mixture 1C-MIM. Individual reagents to generate 1C-MIM are not exclusive and available elsewhere.

Data and code availability

Metabolomics.

- Data depository, Mendeley Data : https://doi.org/10.17632/ghjgddwfzz.1.
- RPC strategy for metabolomics, https://doi.org/10.17632/zgftdrtrxx.1.

Transcriptomics.

- Data depositories: assigned GEO accession numbers as appended below:
  * Database GEO: GSE155193 for myoblast differentiation.
  * Database GEO: GSE145897 for neural stem cell transitions
- Database GEO: GSE229533 Effect of metabolite intervention in mice muscle gene expression
- Database GEO: GSE229534 Effect of metabolites supplementation on C2C12 gene expression

No original code was generated in this study.

Any additional information required to reanalyze the data reported in this work paper is available from the lead contact upon request.

METHOD DETAILS

Animals

ICR mice were purchased from Envigo and the colony was maintained and expanded at Salk Institute animal facility. C57BL mice were purchased from The Jackson Laboratory and the colony was maintained and expanded at both Salk Institute and Altos Labs animal facilities. Mice were utilized for *in vivo* interventions and primary culture assays. For *in vivo* interventions, the gender and age of animals are detailed according to the study sections. All animal handling was approved by the IACUC committee to conform to regulatory standards.

In vitro cell lines and primary cultures

All cell cultures below described were maintained under standard incubation conditions: 37°C in 5% CO_2, 95% humidified air. All cell cultures were authenticated by periodic PCR checks against mycoplasma. Viability and cell number were determined as required by trypan blue and the TC10 Automated Cell Counter (BioRad), New-Bauer chamber, or DeNovix automatic system, according to availability. To ensure the collection of good fractions of viable cells for downstream analysis, the viability of samples was recorded. Most viability readouts were assessed by trypan blue at the time of sample collection. The confirmation of viability was originally needed to account for the strong impact that dead cells can have on RNAseq readouts. In most of the cases, cells were seeded in a 6-well-plates format. On the day of collection, several sterile 15mL tubes were placed on ice (to avoid degradation during the time needed to collect all samples). The original medium from each well was collected into their respective sterile tube (to avoid washing out the dead cells, and truly determine potential toxicity by the treatment). Then 500μL/well of TrypLE was added and plates incubated for 5 min at 37°C. Once cells were detached, the TrypLE-solution (with cells in it) was collected into their respective tube. One additional

wash with 1mL of PBS per well was performed and the wash was collected in their respective tube. Tubes were centrifuged at 300 g × 5 min, and the supernatant was discarded. Each pellet was resuspended with 1mL medium and cells were counted using trypan blue.

Myoblast-cell line culture and differentiation

Myoblasts (C2C12 from ATCC, Cat. CRL 1772) were cultured in Myoblast medium (DMEM with 20% FBS) up to approximately 50% confluency. Cells were detached for passaging using TrypLE according to growth status. For differentiation, when cultures became fully confluent, were washed with PBS, and the above Myoblast medium was replaced by Myofiber differentiation media (DMEM, 2% FBS). Cell morphology was monitored using an IX51 inverted microscope (Olympus).

Primary myoblasts

Myoblasts were isolated from 5-week-old female mice. The hindlimb skeletal muscles were minced and digested in type-I collagenase (Worthington Biochem Cat. LS004194) and dispase B mixture. The digestion was stopped with F-10 Ham's medium containing 20% FBS, and the cells were filtered from debris, centrifuged, and cultured in growth media (F-10 Ham's media, 17% FBS, 4 ng/mL bFGF and 1% penicillin-streptomycin) on uncoated dishes for three days when 5 mL growth media were added each day. Then the supernatant was collected, centrifuged, and resuspended with 0.25% trypsin. After washing off the trypsin, primary myoblasts were seeded on collagen-coated dishes, and the growth medium was changed every two days.

Primary NSCs

NSCs were derived from murine embryonic cortex at 14.5 embryonic days (vaginal plug considered 0.5-day). A single-cell suspension was seeded in anti-adherent solution-treated dishes with Neurobasal medium supplemented with 1X B27 (Life Technologies, Cat. 17504-044) and rh-EGF (Thermo Fisher Scientific, Cat. PH G0311) and hFGF2 (Joint Protein Central, Cat. BBI-EXP-002) (20 ng/mL). Primary neurospheres appeared after 5–6 days of culture and were used only during the first 10-passages. Cultures for NSCs were seeded at 200,000 cells/mL and maintained on standard conditions.

Astrocyte cultures

Astrocytes were derived from cortical tissues postnatal or differentiated from dissociated neurospheres after a second or third passage, generated as described before. For postnatal astrocytes, cortices were isolated from P4 mice pups to get single cells, and cells were sorted with Anti-GLAST (ACSA-1) (MILTENYI BIOTEC, Cat. 130-095-825). Microbead kit according to manufacturer instructions. Cells were plated over pre-treated Poly-L-Lysine plates or Poly-D-Lysine glass-coverslips using Astrocyte Differentiation Medium (DMEM-F12, 10% FBS, 1X B27, and 1X Glutamax). The medium was replaced every other day until day-8 when astrocytes reached a mature phenotype corroborated by immunocytochemistry.

Neuronal cultures

Primary neurons were obtained from the cortex of E14.5 mice brains. Brain dissection was performed in a cold solution of 2% glucose in PBS. Then, tissue was trypsinized, and the suspension was transferred across a 40μm cell strainer to get a single-cell suspension. Cells were plated in a ratio of 800,000 cells per each 22mm poly-D-lysine coverslip with Neuron differentiation medium (Neurobasal media, 1X B27, and 1X Glutamax) and maintained on standard conditions. The half volume of culture media was replaced every other day. Note: In previous studies, we tracked the disappearance of the proliferative neuronal progenitors present in the primary culture by 10μM EdU-pulses every day after plating, and we found that 5-day after seeding, the percentage of EdU+ cells was reduced to basal levels. At this time point, we consider neurons as post-mitotic.

Primary culture of chondrocytes

Primary chondrocytes isolated from femoral and tibial condyles of 5 days old mice were cultured overnight at a density of 7x10^3 cells/cm^2. Chondrocyte medium contains DMEM plus 10% FBS, and 1X Glutamax. The media was replaced the following day with fresh media. Cultures were fed every other day.

MSC-cell line culture and chondrocyte differentiation

MSCs from Cyagen (OriCell Strain C57BL/6 Mouse Adipose-Derived Mesenchymal Stem Cells, Cat. C57BL/6) were thawed in StemXVivo medium and expanded using MSC-Maintenance Medium (alpha-MEM, 10% FBS, and 1X Glutamax). MSCs were differentiated into chondrocytes by using StemPro Chondrogenesis Differentiation Kit (Thermo Fisher Scientific, cat. A10069) by the 3D-culture system during the needed times (as indicated in the corresponding figure legends). Briefly, 2.5 x 10^6 MSCs were resuspended in Chondrocyte differentiation medium and pellet down in 15 mL polypropylene tubes, then, the caps were loosened, and the tubes placed on a rack and incubated in standard conditions. Half of the media was replaced every other day.

Mouse embryonic stem cell culture and trophoblast differentiation

ZHBTcH4 ESCs (Laboratory of Dr. Hitoshi Niwa) were cultured on gelatin-coated plates via standard medium containing fetal bovine serum and LIF. For trophoblast differentiation, ZHBTcH4 ESCs were cultured in the presence of 2 μg/mL Dox to repress Oct-3/4 expression.

Human embryonic stem culture and cardiomyocyte differentiation

Human embryonic stem cell (hESC) H1 line was obtained from WiCell Research and maintained on feeder-free plates pre-coated with Matrigel (BD Biosciences) using mTeSRTM1 media (STEMCELL Technologies Inc.). The cardiomyocyte differentiation was derived from hESCs. In short, dissociated hESCs were seeded on Matrigel pre-coated dishes in mTeSR media in the presence of ROCK inhibitor Y-27632 (Reagents Direct,Cat. 53-B85-50). A GSK inhibitor, CHIR (Selleck, Cat. S2924) was applied for 24 h, followed by addition of the canonical Wnt-signaling inhibitor, IWP4 (Stemgent, Cat. 04–0036). During differentiation, cells were cultured in RPMI medium plus B-27 Supplement.

Human derived-ESC astrocytes

To get neural precursor cells (NPCs), human ESCs (Cat#WA01) were dissociated into single cells by accutase, seeded at 20,000 cells/cm^2 density on matrigel-coated plates and cultured in mTESR1 medium containing 1:100 of Rock inhibitor overnight. Next day, the medium was switched to N2B27-medium (DMEM/F12, 1X N2, 1X B27, 1X Glutamax, 1X NEAA, β-mercaptoethanol [1:1000], and 25 μg/mL insulin), supplemented with the small molecules SB431542 (Tocris, Cat. 1614) 10μM and LDN193189 (Miltenyl Biotec, Cat. 130-106-540) 1μM. Medium was changed daily until day-8 when SB431542 and LDN193189 were withdrawn. On day-14, cells were dissociated and further maintained at high density, grown on matrigel in NPC-medium (DMEM/F12, 1X N2, 1X B27, and 20 ng/mL bFGF), and split every week. Second, for NPC-Astrocyte differentiation, NPCs were plated at 15,000 cells/cm^2 density on matrigel-coated plates in NPC-medium containing 1:100 of Rock inhibitor. Following day after seeding, NPC-medium was switched to astrocyte medium (2% FBS and astrocyte growth supplement). Cells were fed every 2-day for 30-day. Cultures were passaged at a 90–95% confluency.

Human BJ-fibroblasts

BJ skin fibroblast cells were obtained from ATCC (Cat. 27CRL-2522) and grown in DMEM supplemented with 10% FBS, 1X Glutamax, and 1X MEM-NEAA.

Metabolome analysis

Sample collections. Cells and media were collected according to the required time as NSCs, MSCs, and Myoblasts or during their respective differentiation conditions. Each sample was derived from a cell pellet of 100μL-mass-volume measured by the Eppendorf microtube scale. After the indicated time, cell metabolism was stopped by placing cells on an ice-bed, where cells were collected. Cells were scraped from wells, centrifuged 300*g*, 5min, at 4°C, and pellets were flash-frozen in LN2 until further processing by Metabolon company.

Processing of samples at Metabolon

Briefly, samples were homogenized and subjected to methanol extraction then split into aliquots for analysis by ultrahigh performance liquid chromatography/mass spectrometry (UHPLC/MS) in the positive (two methods) and negative (two methods) mode. Metabolites were then identified by an automated comparison of ion features to a reference library of chemical standards followed by visual inspection for quality control. For statistical analyses and data display, any missing values are assumed to be below the limits of detection. Statistics was performed in ArrayStudio (Omicsoft) or "R" to compare data between experimental groups; $p < 0.05$ is considered significant and $0.05 < p < 0.10$ to be trending. An estimate of the false discovery rate (Q-value) is also calculated to take into account the multiple comparisons that normally occur in metabolomic-based studies, with $q < 0.05$ used as an indication of high confidence.

Determination of metabolomic patterns. The relative intracellular abundance of metabolites was estimated as Scaled Intensity, where each value is normalized by Bradford protein concentration before being considered (n = 5 biological replicates). Then, the calculated averages of the scaled intensity of 5 replicates per condition were plotted (on axes 'y') against a continuous scale of time (on axes 'x') according to the collection times determined for each cell type. Metabolites were classified and sorted according to fixed parameters by the Recurrent Pattern Classification Strategy, provided in Data S1, as standalone zip file. Note regarding the comparison of metabolomic bell-patterns: Briefly, the comparison was performed in three different progenitor cell types when those cells were exposed to differentiation conditions. Considering the variation of time span in which each cell type reaches full differentiation (being longer for the differentiation from MSC into chondrocytes and shorter for the NSC and MBs models), this makes the early intermediate transition also slightly different. Therefore, to be able to select a comparable time point between the three cell types, we selected 6h, as it is a balanced time for including the three cell types.

Hierarchical cluster analysis (HCA), K-means clustering, and silhouette analysis

Data used correspond to the values of Bradford-normalized median-Scaled value of each metabolite from 5 biological replicates. Those analyses were conducted using the MeV software. For the clustering analysis of the metabolites profile, the k-means algorithm was performed in R. Briefly, normalized metabolite values for each cell sample were analyzed using the silhouette method to determine the optimal number of clusters. Then, the K-means algorithm was performed with the optimal number of clusters to group the metabolites based on the patterns in metabolite expression levels.

Enrichment analyses. The analyses were performed using the Enrichment Analysis tool of MetaboAnalyst, where we used only the metabolites recognized by the Human Metabolome DataBase (HMDB IDs), with the library Pathway-associated metabolite sets (SMPDB). Consideration: a fraction of metabolites recognized in the Metabolon database are novel and do not have correspondent identifier in the Human Metabolome DataBase (HMDB IDs). The representations were obtained using Excel, GraphPad Prism 8 software, RAW graphs software, and Adobe Illustrator.

Concentration tests of components of one-carbon-metabolite induction medium (1C-MIM)

Cocktail's customization was performed in myoblasts C2C12 and primary cultures of astrocytes.

For astrocytes, cultures tested individual metabolites at different concentrations in a serum-free medium (base media, BM). BM contained equivalent volumes of DMEM-F12 and Neurobasal, plus the supplements N2 (Life Technologies, Cat. 17502048) and B27 at 1X. Only for customization purposes, we observed the relative gene expression of *Gfap*, primary marker of astrocytes, against the exposure of a range of concentrations of each of the components for 1C-MIM. The tracking of this gene expression was performed only to observe

trends to select an appropriate concentration, *i.e.*, not lethal and with a discernible effect in gene expression compared with controls. S-adenosylmethionine (SAMe, Cayman Chemical, Cat. 16376) at millimolar concentrations was lethal for astrocytes, which is in line with the lower physiological concentrations usually found for this metabolite compared to others. Cysteine is highly sensitive to oxidation (manifested as white flake precipitation), then a high-concentrated stock solution [2500mM] (Sigma, Cat. C7477) dissolved in ddH_2O with pH slightly acid (~6) was prepared to prevent this issue. We corroborated a pH always close to 7.4 in the cells maintained *in vitro* (*i.e.*, after adding the 1C-MIM as a cocktail) before and after treating them with cocktails containing the diluted solution of cysteine. Because the growth factor bFGF was added to improve survival (only for astrocytes), we also perform a curve of different concentrations of bFGF; of note, the selected concentration of 20 ng/mL did not inhibit *Gfap*, and lower concentrations even potentiate the expression of *Gfap* (this effect is different from the overall effect of the 1C-MIM cocktail repressing *Gfap*-expression). We tested the mixture of all elements at 1mM, 2.5mM, and 5mM, except for SAM, which was provided at 0.1mM, 0.25mM, and 0.5mM, respectively (*i.e.*, in a ten-times less concentrated compared with the other metabolites). This cocktail represents the 1C-MIM6 with 6 metabolites. Despite that the range of 1mM with separate metabolites like putrescine or threonine (Sigma, Cat. P5780 and T8441), repressed *Gfap*, when those were added in combination, the synergic result did not inhibit *Gfap*. From these readouts, we selected the concentration of 5mM for all metabolites, except for SAM, which was added at 0.5mM, because of the toxicity explained above. We evaluated the 1C-MIM of 6 metabolites versus the elimination of SAM (component lethal at high concentrations) and cysteine (component with higher susceptibility to oxidation, but is the only one that potentiated the *Gfap* expression in a dose-fashion). This cocktail represents the 1C-MIM4 with 4 metabolites. For astrocytes, the combination without SAM or cysteine achieved more inhibition of the *Gfap* marker. However, considering that the metabolites were *a priori* selected because they are critical components of the one-carbon network, we tested both combinations in the experiments with other cells. Finally, we evaluated the effect of the addition of a scramble condition of metabolites not related to 1C-metabolism, including arginine, creatine, fructose, histidine, leucine, and valine, as a scramble cocktail of 6 metabolites, added at 5mM (*i.e.*, with similar concentrations than 1C-MIM).

For myoblasts, differentiation was done by reducing the percentage of serum, from 20% to 2%. Myoblasts well supported the addition of a cocktail with six metabolites (1C-MIM6). The individual metabolites were tested in dose-response by Cell Titer Glo as described below. For RNA sequencing C2C12 myoblasts were cultured under growth medium conditions until they reached 90–100% confluence. Then, the medium was changed to a differentiation medium (DMEM supplemented with 2% horse serum) for four days and returned to medium 10% FBS for another four days, for a total of 8 days in culture to reach a differentiated phenotype. On day 8, cells were treated for 72h with or without 1C-MIM cocktail. For the *in vitro* 1CMIM concentration: methionine, threonine, putrescine, glycine, and cysteine were used at 5mM and SAM at 0.5mM. For the scramble combination was prepared with bicine, histidine, glucose, sucrose, raffinose, and sodium bicarbonate at equimolar concentrations as the 1CMIM cocktail described before. After the 72h treatment, the cells were collected in TRIzol reagent for RNA extraction.

CellTiter-Glo Luminescent Cell assay

Cells were seeded on adherent conditions and used when reached a confluence of 80%. As a control, a killing solution with 1% puromycin was added in each assay together with the range of each metabolite tested. Assays were performed in 96-well plates, where each concentration was run in four wells per assay. Then, each assay was run at least 3 independent times. Cell titer Glo solution was prepared according to the manufacturer's instructions, then incubated over the cells for 15 min (cells previously treated with metabolites for 48h), and luminescence-Glo was quantified on a ClarioStar Plate reader.

Proteasome 20S activity

The assay ab112154 was used to determine by fluorometric methods the activity of the proteasome. Briefly, the LLVY-R110 Substrate was prepared with assay buffer according to the manufacturer's instructions. Myoblasts treated with metabolites were incubated with the reagent protected from light. Controls included the reagent without cells, and cells seeded without adding the reagent. Fluorescence intensity by top read was measured at Ex/Em = 490/525nm on a ClarioStar Plate reader.

Immunocytochemistry

Required cells were seeded on Poly-D-Lysine coverslips, washed with PBS, and fixed in 4% PFA (15min). Samples were permeabilized and blocked for 1h in 5% BSA +0.02% Triton X-100; afterward, the primary antibody solution was added in PBS, and samples were kept in a wet chamber overnight. The next day, samples were washed with PBS +0.2% Tween 20 and incubated with a secondary antibody solution in PBS for 1h. DAPI-Vectashield was used to mount the samples. For myoblasts, after fixation, cells were blocked with 5% goat serum, 2% BSA, 0.2% Triton X-100, and 0.1% NaN_3 in PBS for at least 1h; then the samples were incubated with primary antibodies overnight. After washing with PBS, the samples were incubated with respective secondary antibodies and DAPI for 45 min at room temperature. Images were acquired using a Zeiss LSM 710 Laser Scanning Confocal Microscope (Zeiss). For quantification purposes, the percentage of cells positive to each marker was calculated regarding the total cell number identified by DAPI nuclei, from at least five pictures obtained from each sample. Images were processed with NIH ImageJ software (https://imagej.nih.gov/ij/index.html). Primary antibodies used include anti-Nestin from Millipore (MAB353), anti-Pax7 and anti-MF20 from DSHB (Cat. AB_528428 and AB_2147781), anti-MyoD from Santa Cruz (Cat. sc-377460), anti-Ki67 from Cell Signaling (Cat. 12202), Alexa Fluor 568 and 488 (Cat. A10042, A21134, A11039, and A21206).

Relative measurement of methionine and S-adenosylmethionine

Cells treated under the respective conditions were collected (at least 250,000 cells per each technical replicate). Pellets were flash-frozen and stored in LN2-tank until processed. We lysed and processed the cell pellets according to kit's manufacturer instructions either for methionine quantification (Methionine Assay Kit, fluorometric, Abcam, ab234041) or for SAM quantification (S-Adenosylmethionine ELISA Kit, Cell Biolabs, STA-672).

RNA isolation and gene expression analysis by RT-PCR

Total RNA was isolated at the needed time points, using the RNeasy Plus Mini kit QIAGEN (Cat. 74106), according to the manufacturer's protocol, including a DNA-removal step with DNAseI. Amount and purity of RNA were assessed using a NanoDrop spectrophotometer (Nanodrop Technologies); at least 500ng of total RNA was used to synthesize cDNA by reverse transcription, using Maxima H Minus cDNA Synthesis Master Mix (Thermo Fisher Scientific, Cat. M1662). 2.5–10ng of cDNA was used in the following qPCR performed on a CFX384 thermal cycler (Bio-Rad) using the SsoAdvanced Universal SYBR Green Supermix (BIO-RAD, Cat. 1725274). Results were normalized to at least one reference genes (*β-Actin*, *RPL38*, *GAPDH*, *Gus*, *CTCF*, and *Nat1*, specified per figure), selected for their highest stability among a pool of common housekeeping genes. Primers sequences in Table S5. Statistical analysis of the results was performed using the 2ΔCt method. Results were expressed relative to the expression values of the experimental control.

Transdifferentiation experiments with 1C-MIM treatment

For transdifferentiate MSCs to myofibers, we constructed a MyoD overexpression AAV vector by inserting MyoD-2A-GFP cDNA into an AAV vector (AAV2 inverted terminal repeat vector) under the control of CAG promoter (Vector Biolabs Cat#230116). We initiated the transdifferentiation of MSCs to myocytes by adding 1x10^9 GC AAV-MyoD-2A-GFP and metabolites to the differentiation medium (DMEM with 2% FBS). The control cells were only treated with 1x10^9 GC AAV-MyoD-2A-GFP. At day 4, 6, and 8 post-differentiation, the cells were fixed with 4% PFA and processed for immunofluorescence. Myocytes were recognized by the myosin-heavy chain, which was labeled by MF20.

For transdifferentiate BJ-fibroblast into neurons, the first cell type was transduced with lentivirus containing doxycycline-inducible Neurogenin and rTA. The recombinant AAV vector was generated following the procedures of the Gene Transfer Targeting and Therapeutics Core at the Salk Institute for Biological Studies. Two days post-transduction cells were plated in desired density and treated with metabolites cocktail (MIM4 or MIM6) for 5-day followed by the addition of doxycycline at a concentration of 0.5 μg/mL for induction of Neurogenins for 3-day, then collecting the cells for RNA analysis.

In vivo intervention

C57BL or ICR mice were allocated into groups according to their age, gender, and strain, where possible siblings were split into control and treatment to reduce differences. All mice used in the experiment were wild-type, with no evident health problems. We used mice between 3-4-months-old for experiments for the young phenotype, and mice between 17 and 20-months-old for experiments for the old phenotype. All animals were weighed at the beginning and end of the intervention. The drinking solution was prepared from the stock of water provided by the animal facility, for both controls and supplemented animals. A volume of 150mL of water was provided every other day for each cage containing 5 mice maximum. The remaining volumes of control and supplemented water were measured every time before discarding the remaining volumes and the volume consumed was correlated to the number of mice present in each cage, to determine the drinking volume. The treated water supplementation was delivered in sterile red bottles for a period of one to three months. After these interventions, mice were habituated to walking around an open field test every other day for a week before the muscle injury.

Muscle injury by cardiotoxin

A solution of cardiotoxin (Latoxan S.A.S. Cat. L8102) was prepared at a concentration of 10μM. For old-phenotype, a volume of 50μL was injected into both back legs in the tibialis anterior (TA) and in gastrocnemius (GAS) muscles, using a 29-gauge insulin syringe. For the young phenotype the injection was in TA, GAS, and quadriceps. To provide the injection mice were anesthetized using an isoflurane chamber, afterward, legs were shaved to facilitate the visualization of muscle at the injection time. Mice were allowed to recover over a warm bed set at 38°C for 30 min and then returned to their usual housing when they were awake.

Open field tests

For pre-conditioning and for evaluation after muscle injury, animals were set in the behavioral room for 1 h in advance to habituate them. Next, each animal was placed in its respective chamber to monitor its physical activity. The chamber for recording was connected to the Activity Monitor Software to quantify distance and movements including distance, velocity, resting time, and jumps. Representative snapshots in real-time were taken for a visual representation of the distance traveled, and the raw data was further analyzed using the Activity Monitor and Excel Software.

Immunostaining and HE-staining

After euthanasia muscles from the injury site tibialis anterior (TA) and gastrocnemius (GAS) were collected and frozen in OCT for further sectioning. Transversal sections from both control and treated were obtained using a Leica cryostat set at 10μm thickness. We arranged three slices of muscle per glass slide for downstream experiments. Briefly, muscle slides were fixed with 4% PFA solution, washed with PBS, and cleared with incubation of 100mM Glycine (Sigma, Cat. G5417) for 15 min. Then, samples were blocked and permeabilized (5% goat serum +0.02%Triton X-100 + 0.01% NaN_3 + 2% BSA, in PBS) for 1h at room temperature followed by an overnight incubation with the needed primary antibody at 4°C. The next day, samples were washed with PBS+0.02%tween 20 at least three times, afterward, were incubated with the respective secondary antibodies and DAPI for 1h at room temperature. All secondary antibodies were diluted at a ratio of 1:500. Fluorescent images were captured using a confocal scanning microscope. Quantification using the ImageJ software. For H&E staining we incubated slides into hematoxylin for 5-min and eosin for 3-min, with clearance with ammonium hydroxide solution (1:500), followed by standard washes. Images were captured using bright field microscopy.

Myofibers area measurement

Muscles processed by cryostat as described above were utilized to capture images in Axioscan. For analysis of area of individual myofibers the software ImageJ was used and area of at least 50 center-nucleated myofibers per slice were measured. Then an automatic subdivision per ranges was performed by the Prisma software and using those ranges the averages were estimated per condition.

Single myofiber isolation

EDL muscles were extracted and carefully digested with 2 mg/mL collagenase type I in DMEM (Worthington Biochem) for 45 min at 37°C. Digestion was stopped with a medium containing horse serum. Myofibers were released by gently flushing with a large bore glass pipette. Released single myofibers were treated with 1C-MIM or control medium and 3 days later fixed with 4%PFA for subsequent immunostaining.

DNA-methylation clock from quadriceps

After euthanasia muscles quadriceps (*i.e.*, from non-injury-site) were extracted and flash-frozen and minced in liquid nitrogen, then samples from 25 to 50 mg of ground frozen tissue were separated for genomic DNA extraction. DNA was processed by the Clock Foundation (https://clockfoundation.org/data-tools/),[43] which retrieved the averaged results of three-biological replicates per condition.

RNA-sequencing from quadriceps

After euthanasia muscles quadriceps (*i.e.*, from non-injury-site) were extracted and flash-frozen, and minced in liquid nitrogen, then samples from 50 to 100 mg of ground frozen tissue were separated for RNA extraction. The processing from total-RNA extraction, library prep, sequencing, and analysis was performed at the company Active Motif (https://www.activemotif.com) according to their standard procedures.

RNA-sequencing from *in vitro* cells

Cells were collected at required times and treatments. Cell pellets were lysed with 1mL of Trizol and stored at −80°C for subsequent RNA extraction. Bulk-RNA analysis of astrocytes was developed at Salk Institute; analysis of myoblast at Altos Labs. Analyses of data were performed in BasePair software following the pipelines 'DESeq2, compare 2 groups' or 'DESeq2, 3+groups comparisons'. Further analysis like differential mRNA genes, we tested whether each had enriched GO terms in biological processes and molecular functions using the ToppGene Suite and Gene Set Enrichment Analysis (GSEA) software. For ToppGene, only those functional annotation terms associated with the various sets of differentially expressed genes were clustered that were significantly enriched (Bonferroni correction, $p < 0.01$) compared with the function annotation terms associated with the total population of genes. Biological interpretations and visualizations of differentially expressed genes by using EnrichR and gProfiler.

Re-analysis of *in vitro* canonical partial reprogrammed astrocytes

We re-analyzed RNA-seq data from a previous study tracking the induction of pluripotency in astrocytes through a neural stem cell-like state NCBI Database GEO: GSE69237. We acquired the raw sequencing data and performed differential expression analysis to compare to our 1C-MIM treatment in astrocytes.

Quantification of histone modifications

Bulk histones were acid-extracted from cell pellets, propionylated, and subjected to trypsin digestion. Histone peptides were resuspended in 0.1% TFA in H_2O for mass spectrometry analysis. Samples were analyzed on a triple quadrupole (QqQ) mass spectrometer (Thermo Fisher Scientific TSQ Quantiva) directly coupled with an UltiMate 3000 Dionex nano-liquid chromatography system. Targeted analysis of unmodified and various modified histone peptides was performed. This entire process was repeated three separate

times for each sample. Data were imported and analyzed in Skyline with Savitzky-Golay smoothing. Each modification was represented as a percentage of the total pool of modifications. The process from the histone extraction to the analysis was carried out by Active Motif, Inc.

QUANTIFICATION AND STATISTICAL ANALYSIS

Statistical analysis applied, exact n values, and precision measures are indicated in each figure legend. All readouts derived from metabolomics are derived from n = 5 biological replicates. For other experiments, refer to each figure legend. No statistical methods were used to predetermine the sample size. Randomization or stratification was not applied. In general, data is shown as averages ±S.D. or S.E.M, as indicated in each figure legend. Statistics were performed using GraphPad Prism Software. Comparisons between two groups were analyzed using t-Test Two-tailed, or one-way ANOVA followed by either Bonferroni or Tukey's *post hoc* test, as appropriate. Frequency distribution plots were obtained by analysis tool in Graph Pad Prism (version 9). The statistics from metabolome analyses were obtained under the Metabolon Portal Software as provided for the company (www.portal.metabolon.com/en). For transcriptomic analyses, R Software (R version 3.5.1) was used for statistics, other details about these analyses are in their respective methods' section. For all experiments, values of $p \leq 0.05$ were considered statistically significant.

Cell Reports Medicine, Volume *5*

Supplemental information

Intervention with metabolites emulating endogenous cell transitions accelerates muscle regeneration in young and aged mice

Reyna Hernandez-Benitez, Chao Wang, Lei Shi, Yasuo Ouchi, Cuiqing Zhong, Tomoaki Hishida, Hsin-Kai Liao, Eric A. Magill, Sebastian Memczak, Rupa D. Soligalla, Chiara Fresia, Fumiyuki Hatanaka, Veronica Lamas, Isabel Guillen, Sanjeeb Sahu, Mako Yamamoto, Yanjiao Shao, Alain Aguirre-Vazquez, Estrella Nuñez Delicado, Pedro Guillen, Concepcion Rodriguez Esteban, Jing Qu, Pradeep Reddy, Steve Horvath, Guang-Hui Liu, Pierre Magistretti, and Juan Carlos Izpisua Belmonte

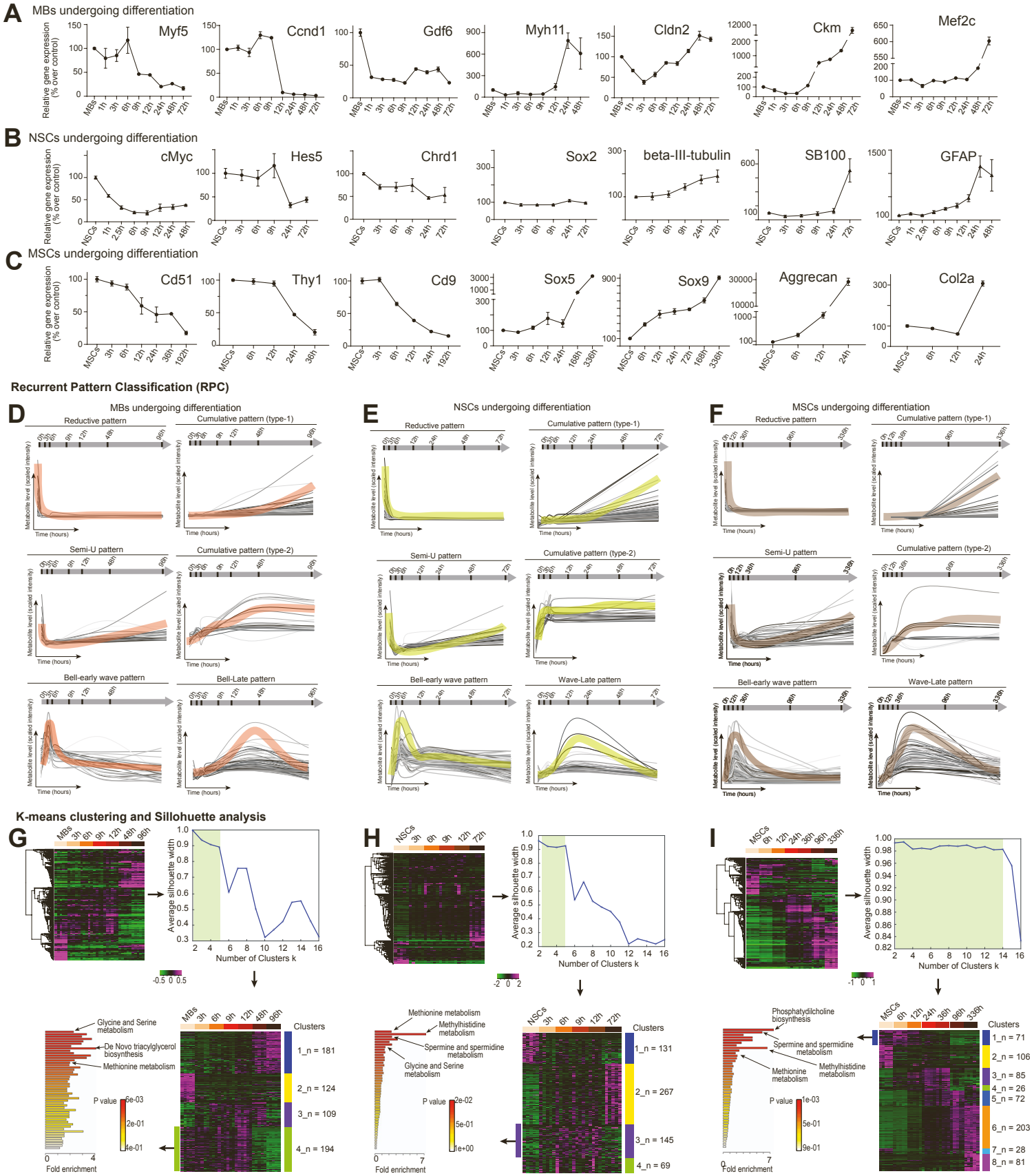

Fig. S1. Comparison of the transitional populations differentiated from MBs, MSCs, and NSCs.
(**A-C**) Reference genes selected to track the transition profile during differentiation of MBs towards myofibers in (A), NSCs towards astrocytes in (B), and MSCs towards chondrocytes (C), represented as percentage over time zero (time 0h= MB-, NSC-, or MSC-steady-state). Total mRNA levels were detected by rtPCR. Expression normalized with the geometric mean of at least two housekeeping genes (from Actb, Gapdh, and Nat1) and then normalized vs. control condition (time=0h). Represented the means ± SEM, n ≥ 3.
(**D-F**) Schematic representation of the abundance patterns of individual metabolites over time. Patterns observed by plotting in a continuous scale of time the mean abundance of each metabolite and then grouped according to the similarity of its behavior on the transitional populations differentiated from MBs in (D), NSCs in (E), and MSCs in (F). Full disclosure of patterns and the algorithms to derive them, in Dataset S1. Gray lines in the background represent each, one metabolite. Colored over line, an illustrative trend. The raw mean values from each metabolite (each gray line) are from n=5.
(**G-I**) Metabolomic analyses in MBs (G), NSCs (H), and MSCs (I). On each panel, hierarchical clustering analysis (HCA) of the fingerprint by time in the transitional populations differentiated from each multipotent stem cells (top left). Following the black arrows, on the side of each HCA, the respective Silhouette analysis (top right; green area indicates predicted appropriate number of clusters), which determines the k-means clustering analysis (bottom right). On the bottom-left panel, the enrichment analysis of selected cluster. Experiments shown are from n=5 biological replicates per cell lineage. Related to Figure 1.

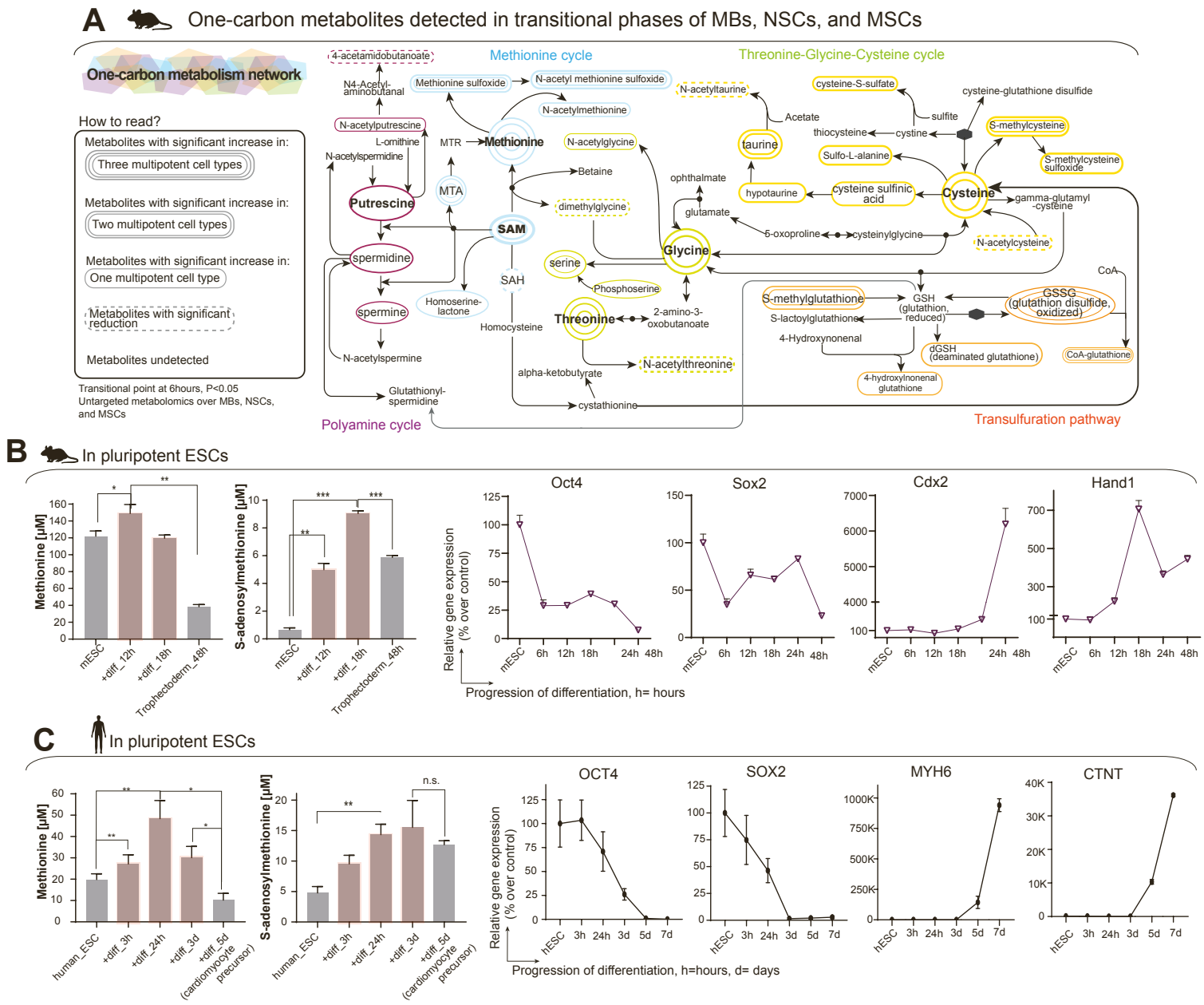

Fig. S2. Common metabolites appear as a wave at the onset of cell identity changes of pluripotent and multipotent cells from mouse and human.

(**A**) Representation of the increase identified in the relative levels of metabolites in three different cell populations derived from MBs, NSCs, and MSCs. Names circled represent metabolites that increase significantly at 6 hours after inducing their differentiation (P<0.05). One, two, or three circles denote significant increases in one, two, or the three cell types, respectively. Dotted circles enclose metabolites that only increase in one cell type, while the other two showed a negative trend. For specific characterization per cell type and times, see Tables S2-S4. Experiments shown are from n=5 replicates per cell type.

(**B**) Quantification of methionine and S-adenosylmethionine (SAM) levels in early states after inducing differentiation of human ESCs to cardiomyocytes; n=3 technical replicates, significantly different at *P<0.05, **P<0.01 (paired t-test). On the right side, as reference for the selection of times, the gene expression of 2-ESC-markers (OCT4 and SOX2) and 2-cardiomyocyte-markers (MYH6, CTNT) measured by rtPCR; where gene expression was normalized to the mean of GAPDH as housekeeping gene, and then normalized vs. control condition (time=0h). Represented the means ± SEM, n = 3.

(**C**) Quantification of methionine and S-adenosylmethionine (SAM) levels in early states after inducing differentiation of mouse ESCs to trophectoderm (cell line Zhbtc4); n=4 technical replicates, significantly different at *P<0.05, **P<0.01 (paired t-test). On the right side, as reference for the selection of times, the gene expression of 2-ESC-markers (Oct4 and Sox2) and 2-trophectoderm-markers (Cdx2 and Hand1) measured by rtPCR; where gene expression was normalized to the mean of Nat1 as housekeeping gene, and then normalized vs. control condition (time=0h). Represented the means ± SEM, n=3.

Means ± SEM, statistically different from controls at **P<0.01, ***P<0.001, and n ≥ 3, where dots represent independent values.
Related to Figure 1.

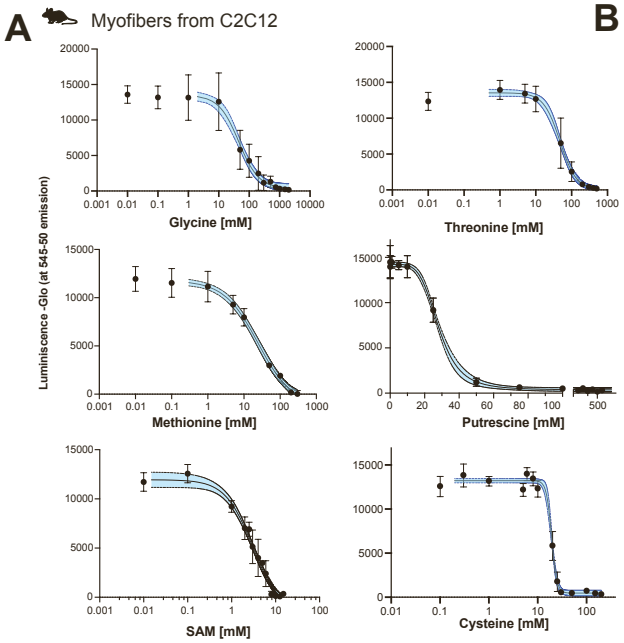

B

Primary Astrocytes

Condition:	Control	0.025mM	0.25mM	2.5mM	5mM	10mM
Metabolite: Glycine						
Gfap relative expression over control	100 ± 4.56	70.19 ± 2.56	68.03 ± 3.65	81.87 ± 6.26	75.96 ± 6.97	73.53 ± 3.16
Metabolite: Methionine						
Gfap relative expression over control	100 ± 2.55	124.22 ± 4.39	105.73 ± 4.73	113.17 ± 12.7	114.89 ± 18.72	117.36 ± 5.9
Metabolite: Putrescine						
Gfap relative expression over control	100 ± 13.14	46.66 ± 1.44	57.03 ± 5.99	48.99 ± 2.27	51.79 ± 4.79	☠ LETHAL
Metabolite: Threonine						
Gfap relative expression over control	100 ± 9.62	22.78 ± 3.78	26..71 ± 2.41	25.13 ± 0.2	22.31 ± 0.08	25.32 ± 0.13
Metabolite: Cysteine						
Gfap relative expression over control	100 ± 5.85	62.89 ± 2.79	78.8 ± 3.05	127.91 ± 2.53	190.68 ± 7.32	227.6 ± 11.27
Metabolite: SAM						
Condition:	Control	0.1mM	0.25mM	0.5mM	2.5mM	10mM
Gfap relative expression over control	100 ± 6.29	30.95 ± 2.79	27.18 ± 1.48	21.46 ± 1.45	☠ LETHAL	☠ LETHAL
No metabolite, but bFGF						
Condition:	Control	1ng/mL	5ng/mL	10ng/mL	20ng/mL	
Gfap relative expression over control	100 ± 7.17	267.5 ± 6.5	163.5 ± 10.5	89.0 ± 8.0	64.33 ± 6.69	
No metabolite (BM)						
Condition:	Control	Base Medium (BM)				
Gfap relative expression over control	100 ± 4.09	82.64 ± 10.04				

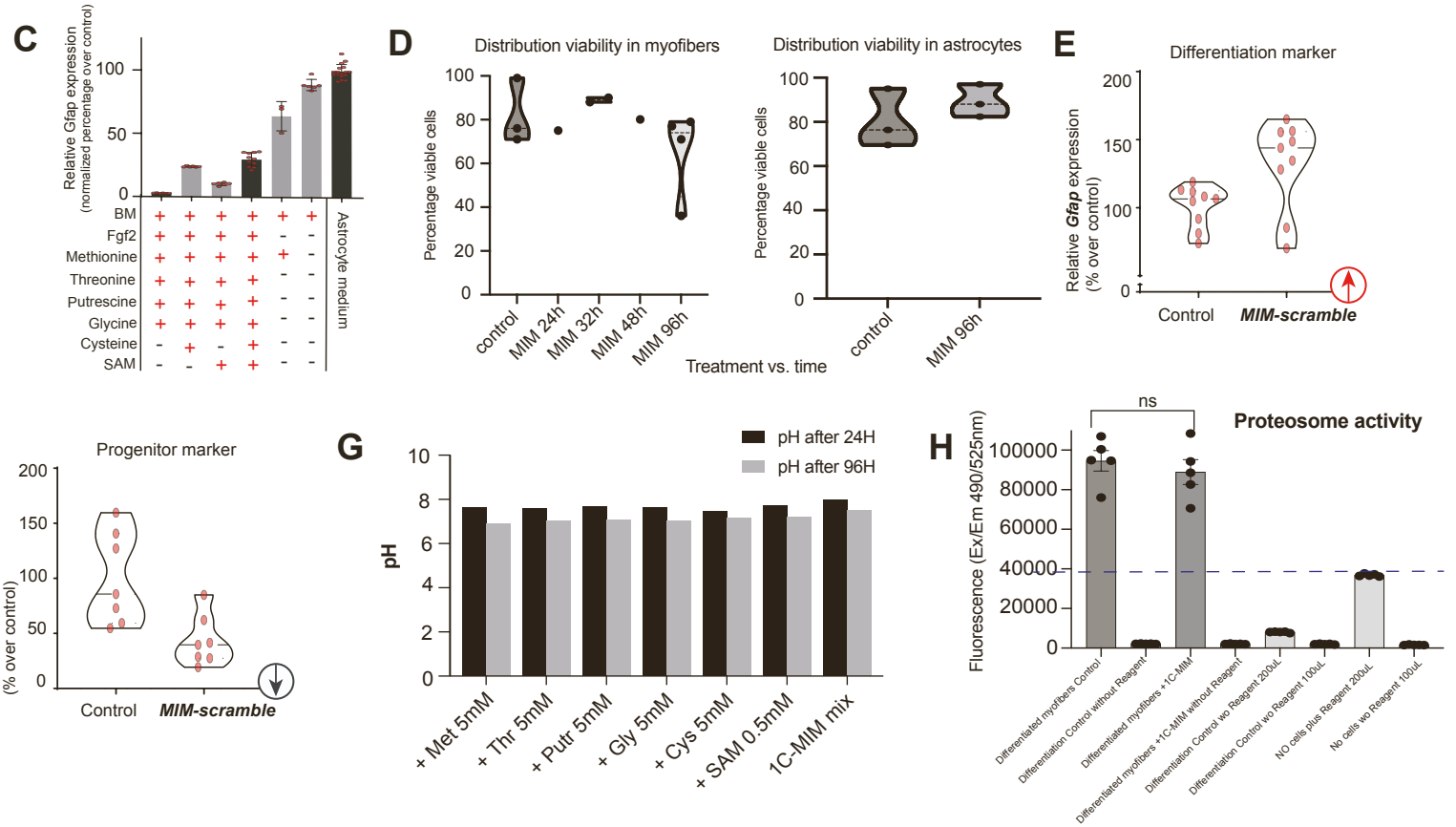

Fig. S3. Standardizations on the supplementation with 1C-metabolites and phenotype changes on differentiated cells.
(**A**) Effect dose-response of individual metabolites over myofibers in vitro, where cell viability is evaluated by the relative quantification of ATP present by a luminescent assay, as an indicator of metabolically active cells.
(**B**) Effect dose-response over the astrocytic phenotype evaluated by levels of expression of the glial marker GFAP; the expression was normalized with the geometric mean of at least two housekeeping genes (from Actb, Gapdh, and Nat1) and then normalized vs. control condition. Dots represent each value ($n \geq 5$), and bars the mean ± SEM.
(**C**) Comparison of 1C-MIM of 6 metabolites (MIM6) versus the elimination of SAM (component lethal at high concentrations) and (or) cysteine (component with higher susceptibility to oxidation), see details in methods. The cocktail without SAM and without cysteine represents the 1C-MIM4 with 4-metabolites. Standardizations were done in mouse astrocytes. Note that the combination without SAM or cysteine achieved more inhibition of the Gfap-marker; thus, both combinations were tested, as seem to be dependent on the cell type.
(**D**) Quantification of viable cells by trypan blue exclusion on myofibers (left panel) and astrocytes (right panel).
(**E**) Evaluation of the effect of a scrambled mixture of metabolites not related to 1C-metabolism. This includes arginine, creatine, fructose, histidine, leucine, and valine; metabolites were added at 5mM (i.e., with similar concentrations than 1C-MIM). Note that scramble-cocktail did not lower Gfap-differentiation-marker neither potentiated the Ascl1-progenitor marker (opposite effect to the observed with 1C-MIM).
(**G**) pH measurements of myoblast in culture in the presence of indicated metabolites (individually or in combination) for 24 or 96 hours.
(**H**) Relative levels of proteosome activation in myofiber cultures supplemented with 1C-MIM, where differences compared with control are significant at **P<0.001 or ***P<0.0001.).
Dots represent each value ($n \geq 5$), and bars the mean ± SEM. Related to Figure 2.

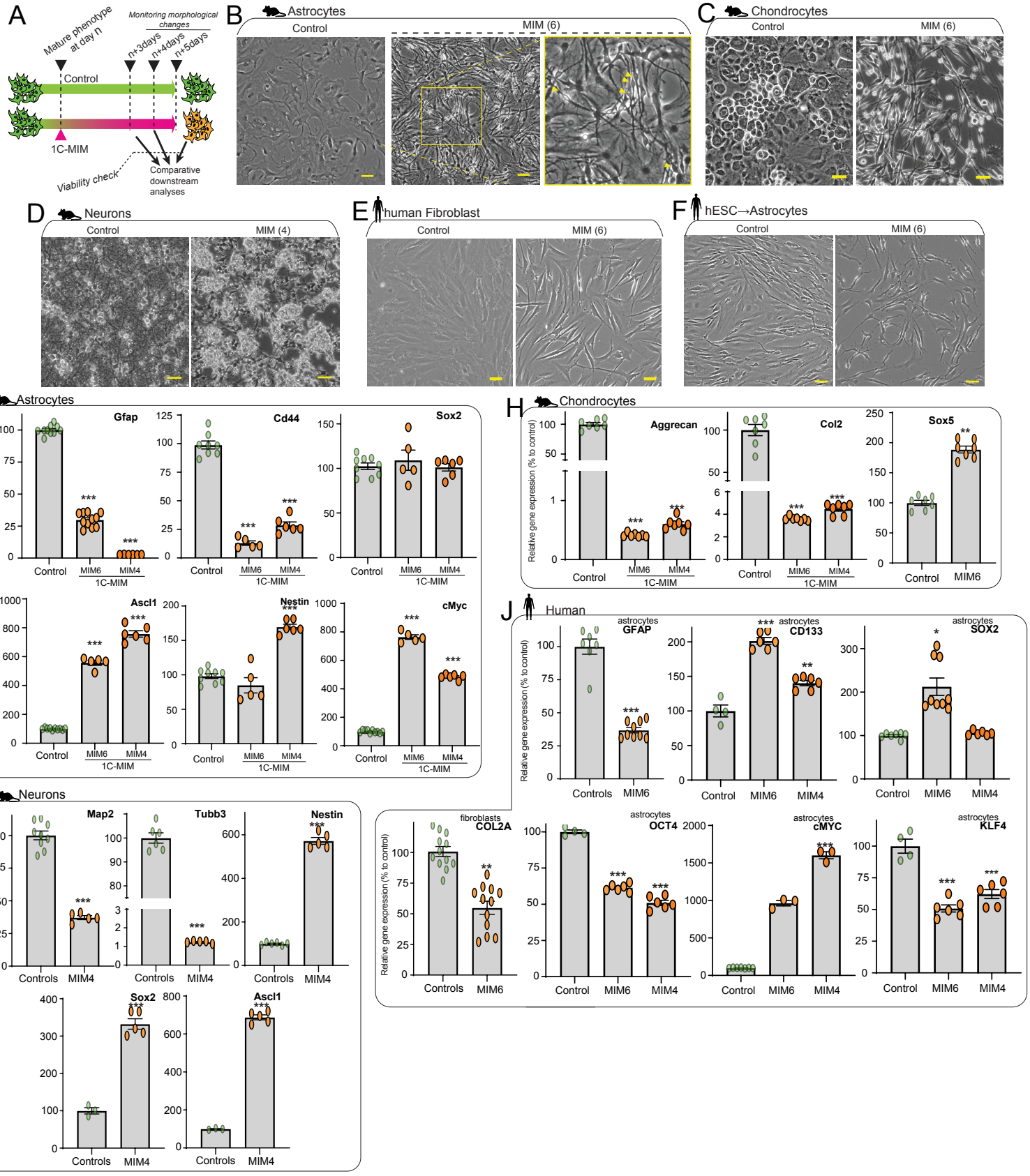

Fig. S4. Basic gene marker screening on differentiated cells treated with 1C-MIM.

(**A**) Experimental setup for supplementation: cells cultured from the same batch are maintained for the time necessary to express mature markers under a differentiation condition (according to each lineage, mature markers expression differs on time, represented in the schema as 'n'). Then cell populations of the same batch are separated and exposed to a control or 1C-MIM-supplemented medium with feeding every other day. MIM6 contains Methionine, Glycine, Putrescine, Cysteine, S-adenosylmethionine; while MIM4 is the former composition minus Cysteine and S-adenosylmethionine. The time for collection was determined in each cell type by observing changes in morphology. For mouse neural-related cells, samples were collected after 4 days of supplementation, for chondrocytes and fibroblasts after 5 days. Note: only muscle cells were collected after 3 days of supplementation (images not presented here, but in the main figure 2). The cell viability was determined at the time of collection as detailed in the Star Methods, and then samples were used for downstream analysis as required.

(**B-F**) Bright-field representative images of cultures of mouse astrocytes, chondrocytes, neurons; and human fibroblasts and astrocytes. Scale bar 50µm. The yellow square in (B) reflects the digital zoom observed in the image located to the right, for details on morphology.

(**G-J**) Representative markers were measured by qRT-PCR in the indicated cell types. The gene expression of genes of interest was normalized with the geometric mean of at least two housekeeping genes (from Actb, Gapdh, and Nat1) and then normalized vs. control conditions. Each dot represents an independent sample (n > 3), where differences compared with control are significant at *P<0.05, **P<0.005, ***P<0.001. Related to Figures 2, 3.

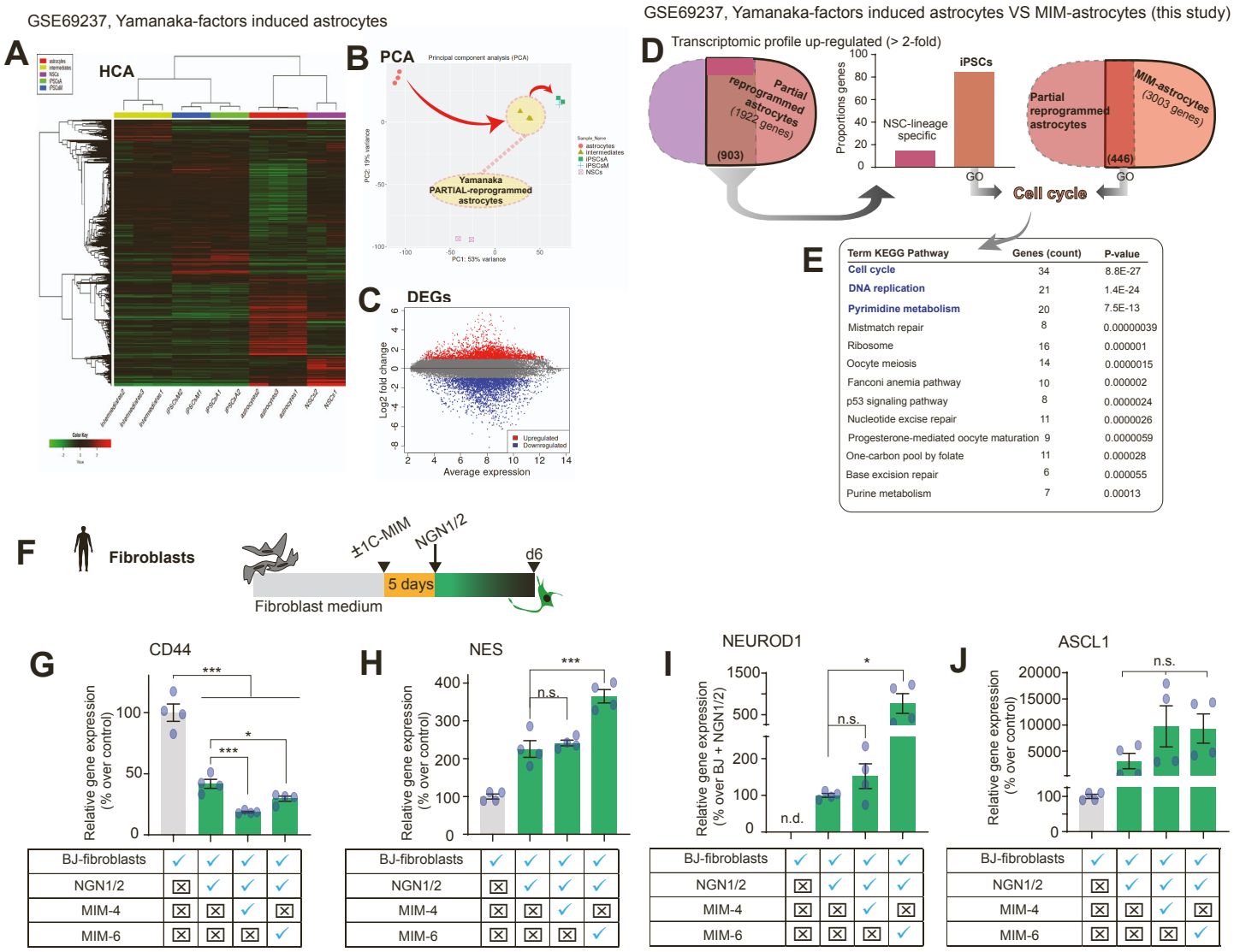

Fig. S5. Orthogonal readouts in astrocytes and fibroblasts corroborate the facilitation of identity transitions by 1C-MIM supplementation in vitro.

(**A-E**) 1C-MIM supplementation induced an intermediate like-progenitor state by regulating cell cycle in astrocytes. In (A) HCA, in (B) PCA, and in (C) volcano plot of DEG. Euclidean distance of RNAseq from astrocytes and intermediate reprogrammed cells (by canonical Yamanaka factors) compared with NSCs and iPSC as reference. The former available database GSE69237 was used to generate these representations. In (**D**) comparison between that former data (GSE69237) and the MIM-astrocytes of this study: where, Venn diagrams show the intersection of the transcriptomic profiles of the indicated populations; and the bars in between represent quantity and type of genes identified in the intersections. Of note 446 genes are shared between partial-reprogrammed and MIM astrocytes; particularly, those genes belong to iPSC-reprogrammed marks and are functionally enriched by Gene Ontology to a cell cycle function as shown in (E).

(**F-J**) Functional assay for the transdifferentiation of human BJ-fibroblasts into neuron-like cells enhanced by 1C-MIM. Schematic representation of the pre-treatment with 1C-MIM before the induction of Neurogenin 1+2 (NGN1/2) in (F). Relative expression of genes for fibroblast-identity in (G) and neuron-identity in (H-J). The expression was normalized with the mean of the housekeeping gene CTCF, then normalized vs. control condition BJ-fibroblasts; except in (l) where NEUROD1 was not detected in fibroblasts and the conditions with MIM were normalized vs. BJ-fibroblast + NGN1/2. Blue dots represent each value ± SEM.

Significantly differences at *P<0.05, **P<0.005, ***P<0.0001. Related to Figure 3.

A

TOTAL mice used in this study	87				
Distribution summary	Control-untreated	1C-MIM-intervention	1C-MIM-intervention-short_term + HIGHdose	Glycine-intervention	Scramble-intervention
	37	30	12	4	4
ROUND 1					
Intervention started at age of 6 weeks-old					
Intervention finished at age of 17.5 weeks-old					
Conditions (MALES strain strain ICR-CD1)	Control-untreated	1C-MIM-intervention			
#mice per condition:	4	5			
ROUND 2					
Intervention started at age of 9 weeks-old					
Intervention finished at age of 22.5 weeks-old					
Conditions (FEMALES, strain ICR-CD1)	Control-untreated	1C-MIM-intervention			
#mice per condition:	3	5			
ROUND 3					
Intervention started at age of 10 weeks-old					
Intervention finished at age of 14.5 weeks-old					
Conditions (BothGenres, strain ICR-CD1)	Control-untreated		Short term +High Dose		
#mice per condition (females):	3		3		
#mice per condition (males);	3		4		
ROUND 4					
Intervention started at age of 9 weeks-old					
Intervention finished at age of 15 weeks-old					
Conditions (MALES, strain ICR-CD1)	Control-untreated	1C-MIM-intervention	Short term +High Dose		
#mice per condition:	10	5	5		
#mice **without injury** per condition:	3	4			
ROUND 5					
Intervention started at age of 9 weeks-old					
Intervention finished at age of 22.5 weeks-old					
Conditions (MALES, strain C57BL/6J)	Control-untreated	1C-MIM-intervention		Gly_intervention	Scr_intervention
#mice per condition :	4	4		4	4
ROUND 6					
Intervention started at age of 72 weeks-old					
Intervention finished at age of 88.5 to 90 weeks-old					
Conditions (MALES, strain C57BL/6J)	Control-untreated	1C-MIM-intervention			
#mice per condition (ended at 88.5wo):	3	3			
#mice per condition (ended at 90wo):	4	4			

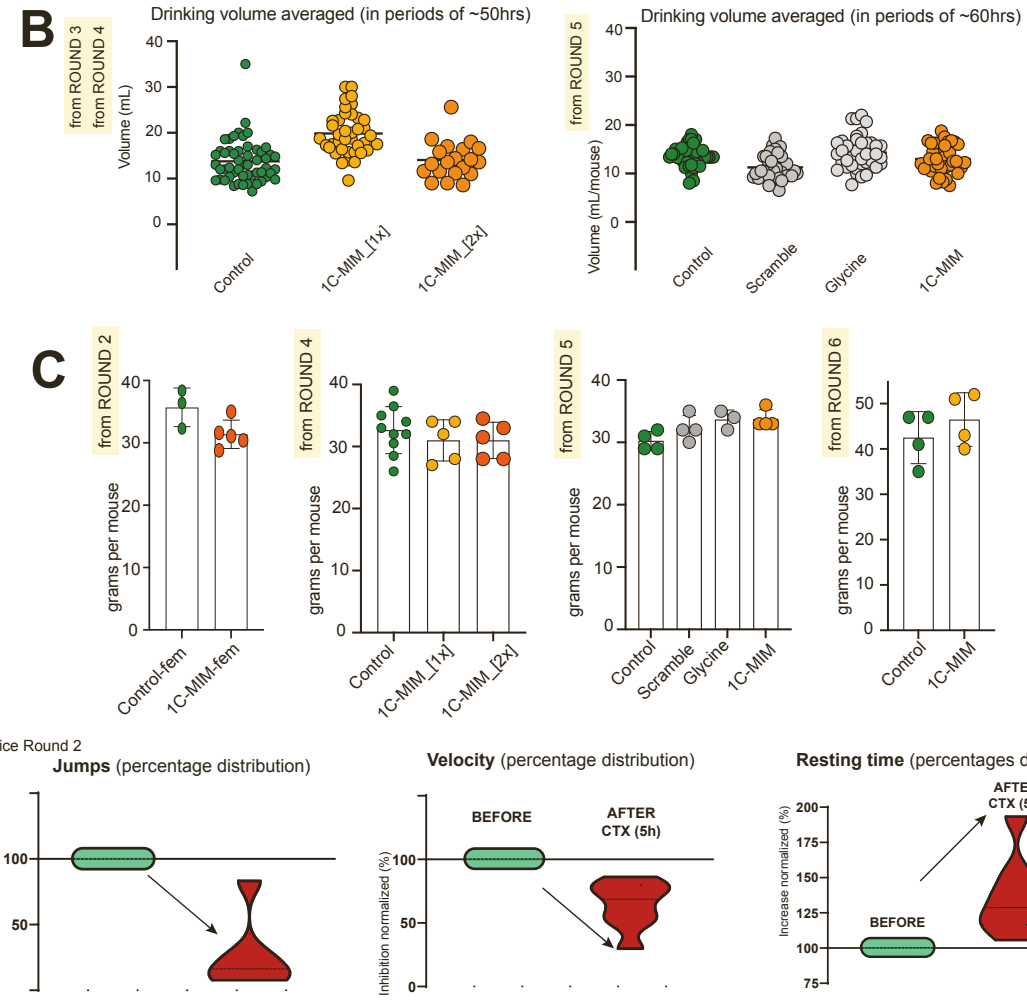

Fig. S6. Experimental design and immediate parameters evaluated for the in vivo intervention with 1C-MIM.
(**A**) Distribution per round of the 87 mice used in the study. Each round represents the experimental intervention used for the study. Only two mice including control and 1C-MIM treated exhibited tumors, and only in the group of aged animals (round 6), therefore no correlation of tumor emergence was associated with the intervention.
(**B**) Drinking volumes. The drinking supplementation was replaced every other day with a standard volume, and measurements of consumption were taken during the intervention. The volumes were normalized according to the number of mice per cage.
(**C**), Bodyweight measurements after 1C-MIM drinking supplementation per round. Each dot represents one mouse.
(**D**) Movement impairment elicited after 5 hours of CTX injection evaluated in terms of jumps, velocity, and resting time. Measurements derived from the Open Field Test, recorded for a period of 60 minutes, graphs represent the distribution including control and 1C-MIM supplemented mice.
Related to Figures 4, 5, 6.

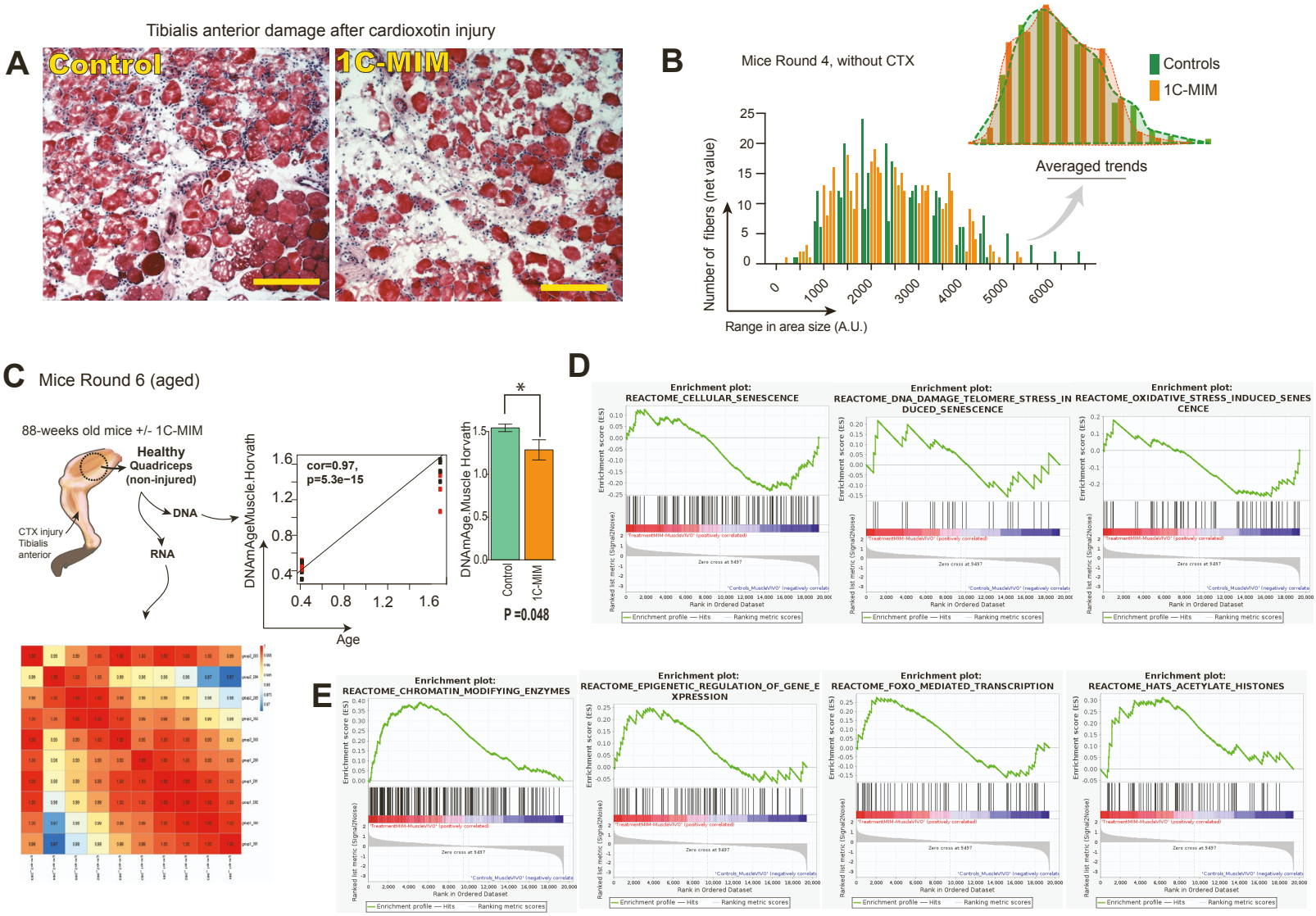

Fig. S7. Analyses on the 1C-MIM intervention in muscle with and without CTX injury.
(**A**) Representative histology images ~5 hours after CTX-injury showing similar damage in control and 1C-MIM supplemented mice. Tibialis anterior sections are stained by H&E (scale bar =250µm).
(**B**) Myofiber size distribution of centrally nucleated fibers without CTX injury of control and 1C-MIM supplemented mice. Insert to the right represents the average.
(**C**) DNA methylation clock using the Horvath Clock demonstrates rejuvenation after 1C-MIM supplementation in quadriceps non-injured. Left panel, schematic representation of how same samples were processed for transcriptomics and methylation, middle correlation analysis; and right panel, estimation of the methylation age using the Horvath clock for muscle. Tissues were recovered at 88-weeks old mice.
(**D-E**) Gene set enrichment analyses from transcriptomic analysis. See also Fig. 6A.

Table S1. Identification of pathways relevant to the intermediate transition (bell pattern). The below pathways represent the enrichments obtained by Metaboanalyst®. Source of the Venn diagram for the intermediate transition.
Experiments were from n=5 biological replicates.
Related to Figure 1G.

MBs, cluster4 (n=194)	NSCs, cluster#3 (n=145)	MSCs, cluster#1 (n=71)
Glycine and Serine Metabolism	Methionine Metabolism	Phosphatidylcholine Biosynthesis
Carnitine Synthesis	Methylhistidine Metabolism	Spermidine and Spermine Biosynthesis
Urea Cycle	Spermidine and Spermine Biosynthesis	Aspartate Metabolism
Glucose-Alanine Cycle	Homocysteine Degradation	Taurine and Hypotaurine Metabolism
Nucleotide Sugars Metabolism	Betaine Metabolism	Phosphatidylethanolamine Biosynthesis
Betaine Metabolism	Taurine and Hypotaurine Metabolism	Phospholipid Biosynthesis
Arginine and Proline Metabolism	Glycine and Serine Metabolism	Arginine and Proline Metabolism
De Novo Triacylglycerol Biosynthesis	Purine Metabolism	Methylhistidine Metabolism
Glutamate Metabolism	Sphingolipid Metabolism	Carnitine Synthesis
Ammonia Recycling	Valine, Leucine and Isoleucine Degradation	Methionine Metabolism
Malate-Aspartate Shuttle	Glutathione Metabolism	Glycolysis
Cardiolipin Biosynthesis	Pantothenate and CoA Biosynthesis	Plasmalogen Synthesis
Plasmalogen Synthesis	Glutamate Metabolism	Urea Cycle
Methionine Metabolism	Carnitine Synthesis	Warburg Effect
Galactose Metabolism	Arginine and Proline Metabolism	Gluconeogenesis
Ketone Body Metabolism	Cysteine Metabolism	Glycine and Serine Metabolism
Glutathione Metabolism	Phosphatidylethanolamine Biosynthesis	Sphingolipid Metabolism
Transfer of Acetyl Groups into Mitochondria	Histidine Metabolism	Beta Oxidation of Very Long Chain Fatty Acids
Phosphatidylcholine Biosynthesis	Selenoamino Acid Metabolism	Mitochondrial Electron Transport Chain
Starch and Sucrose Metabolism	Phosphatidylcholine Biosynthesis	Catecholamine Biosynthesis
Citric Acid Cycle	Ammonia Recycling	Vitamin B6 Metabolism
Beta-Alanine Metabolism	Beta-Alanine Metabolism	Ubiquinone Biosynthesis
Glycerolipid Metabolism	Alanine Metabolism	Purine Metabolism
Glycolysis	Phosphatidylinositol Phosphate Metabolism	Glutathione Metabolism
Aspartate Metabolism	Aspartate Metabolism	Betaine Metabolism
Gluconeogenesis	Nicotinate and Nicotinamide Metabolism	Glutamate Metabolism
Alanine Metabolism	Nucleotide Sugars Metabolism	Estrone Metabolism
Cysteine Metabolism	Catecholamine Biosynthesis	Glycerolipid Metabolism
Homocysteine Degradation	Vitamin B6 Metabolism	Oxidation of Branched Chain Fatty Acids
Mitochondrial Beta-Oxidation of Short...	Ubiquinone Biosynthesis	Mitochondrial Beta-Oxidation of Short...
Warburg Effect	Lactose Synthesis	Phenylalanine and Tyrosine Metabolism
Mitochondrial Beta-Oxidation of Long...	Pyrimidine Metabolism	Mitochondrial Beta-Oxidation of Long...
Pyruvate Metabolism	Transfer of Acetyl Groups into Mitochondria	Starch and Sucrose Metabolism
Pyruvaldehyde Degradation	Estrone Metabolism	Ammonia Recycling
Butyrate Metabolism	Urea Cycle	Citric Acid Cycle
Mitochondrial Electron Transport Chain	Lysine Degradation	Fructose and Mannose Degradation
Ethanol Degradation	Citric Acid Cycle	Amino Sugar Metabolism
Phospholipid Biosynthesis	Fatty Acid Biosynthesis	Nicotinate and Nicotinamide Metabolism
Threonine and 2-Oxobutanoate Degradation	Galactose Metabolism	Tyrosine Metabolism
Glycerol Phosphate Shuttle	Porphyrin Metabolism	Galactose Metabolism
Taurine and Hypotaurine Metabolism	Propanoate Metabolism	Histidine Metabolism
Inositol Metabolism	Pyruvate Metabolism	Fatty acid Metabolism
Methylhistidine Metabolism	Warburg Effect	Pyruvate Metabolism
Caffeine Metabolism	Tryptophan Metabolism	Tryptophan Metabolism
Estrone Metabolism	Bile Acid Biosynthesis	Bile Acid Biosynthesis
Nicotinate and Nicotinamide Metabolism	Tyrosine Metabolism	Arachidonic Acid Metabolism
Phytanic Acid Peroxisomal Oxidation		
Inositol Phosphate Metabolism		
Mitochondrial Beta-Oxidation of Medium...		
Purine Metabolism		

Table S2. Identification of trends of one-carbon metabolites during the intermediate stage between steady-state of Myoblasts (MBs) and early transitional-states of differentiated counterparts. Statistical trends in the relative abundance of individual metabolites at the indicated times. Times selected by their potential overlap with the earliest/immediate transcriptional changes derived from the induction of differentiation. Experiments were from n=5 biological replicates.
Related to Figure 1 and descriptive of Supplemental figure 1D.

PATHWAYS	Comparisons	*Comparison of MBs vs 6 hours of differentiation*	*Comparison of MBs vs 12 hours of differentiation*	*Comparison of MBs at 12 hours of differentiation vs 96 hours differentiation*
Methionine-SAM Metabolism	Significant positive trend (p<0.05)	Cysteine, methionine, cysteine sulfinic acid.	Cysteine, methionine, taurine, homocysteine, cysteine sulfinic acid.	Cysteine-sulfinic acid, SAH, cystine, methionine sulfoxide.
	Positive trend (p<0.10)	Not applicable.	Not applicable.	Not applicable.
	Insignificant change (p>0.1)	SAH, SAM, hypotaurine, N-acetylmethionine, taurine, cystine, homocysteine.	SAH, SAM, cystine, N-acetylcysteine, N-acetylmethionine, N-formylmethionine.	S-methylcysteine, cysteine, S-methylmethionine, S-methylcysteine-sulfoxide, methionine sulfone.
	Negative trend (p<0.10)	N-acetylmethionine sulfoxide.	Hypotaurine, cystathionine.	DMPTA, N-acetylmethionine.
	Significant negative trend (p<0.05)	S-methylcysteine sulfoxide, S-methylmethionine, S-methylcysteine, DMPTA, methionine sulfone, methionine sulfoxide, cystathionine, N-formylmethionine, N-acetylcysteine, N-acetyltaurine.	S-methylcysteine sulfoxide, S-methylmethionine, S-methylcysteine, N-acetyltaurine, methionine sulfoxide, DMPTA, methionine sulfone, N-acetylmethionine sulfoxide.	Methionine, N-formylmethionine, SAM, N-acetylcysteine, hypotaurine, homocysteine, cystathionine, N-acetyltaurine, taurine, N-acetylmethionine-sulfoxide.
Gly-Ser-Thr Metabolism	Significant positive trend (p<0.05)	Threonine, serine, phosphoserine.	Threonine, serine.	Dimethylglycine.
	Positive trend (p<0.10)	Not applicable.	Phosphoserine.	Not applicable.
	Insignificant change (p>0.1)	Glycine	N-acetylthreonine, glycine.	Not applicable.
	Negative trend (p<0.10)	Not applicable.	Not applicable.	Not applicable.
	Significant negative trend (p<0.05)	Dimethylglycine, betaine, N-acetylserine, N-acetylthreonine.	Dimethylglycine, betaine, N-acetylserine.	Threonine, N-acetylserine, serine, betaine, glycine, phosphoserine, N-acetylthreonine.
Polyamine Metabolism	Significant positive trend (p<0.05)	MTA, spermine, spermidine.	MTA, spermine, spermidine.	N-acetylputrescine, putrescine.
	Positive trend (p<0.10)	Not applicable.	Not applicable.	Not applicable
	Insignificant change (p>0.1)	Not applicable.	N-acetylspermidine.	A-acetamidobutanoate.
	Negative trend (p<0.10)	Not applicable.	Not applicable.	Not aplicable.
	Significant negative trend (p<0.05)	4-acetamidobutanoate, N-acetylspermidine, N-acetylisoputreanine, N-acetylputrescine, putrescine.	N-acetyl isoputreanine, 4-acetamidobutanoate, N-acetylputrescine, putrescine.	N-acetyl-isoputreanine, spermine, spermidine, N-acetylspermidine, MTA.
Glutathione Metabolism	Significant positive trend (p<0.05)	Cyclyc dGSH, GSNO, CoA-glutathione, GSSG, S-methylglutathione.	Cyclyc dGSH, GSH, S-nitrosoglutathione, S-methylglutathione, 4-hydroxy-nonenal-glutathione, GSSG,	Cysteine-glutahione disulfide, 5-oxoproline.

CONTINUE TABLE S2

		cysteinglycine, S-lactoylglutathione.	
Positive trend (p<0.10)	Not applicable.	Not applicable.	Not applicable.
Insignificant change (p>0.1)	Cysteine-glutathione disulfide, cysteinglycine, S-lactoylglutathione, 4-hydroxy-nonenal glutathione, glutathione reduced.	Dicarboxylethylglutathione, CoA-glutathione.	CoA-glutathione, 2-hydroxybutyrate.
Negative trend (p<0.10)	Not applicable.	Not applicable.	Not applicable.
Significant negative trend (p<0.05)	Opthalmalate, 5-oxoproline, 2-hydroxybutyrate, dicarboxyethylglutathione.	Opthalmalate, 5-oxoproline, 2-hydroxybutyrate, cysteine-glutathione disulfide.	Opthalmalate, cyclic dGSH, S-lactoylglutathione, dicarboxylethylglutathione, GSSG, GSNO, cysteinglycine, S-methylglutathione, 2-hydroxybutyrate, 4-hydroxy-nonenal-glutathione.

Table S3. Identification of trends of one-carbon metabolites during the intermediate stage between steady-state of Neural Stem Cells (NSCs) and early transitional-states of differentiated counterparts. Statistical trends in the relative abundance of individual metabolites at the indicated times. Times selected by their potential overlap with the earliest/immediate transcriptional changes derived from the induction of differentiation. Experiments were from n=5 biological replicates.
Related to Figure 1 and descriptive of Supplemental figure 1E.

PATHWAYS	Comparisons	*Comparison of NSCs vs 6 hours of differentiation*	*Comparison of NSCs vs 12 hours of differentiation*	*Comparison of NSCs at 12 hours of differentiation vs 72 hours differentiation*
Methionine-SAM Metabolism	Significant positive trend (p<0.05)	SAM, cysteine, methionine, N-acetylcysteine, sulfo-L-alanine, N-acetylmethionine, S-methylcysteine, S-methylcysteine sulfoxide, taurine, N-acetyltaurine, methionine sulfoxide, N-acetylmethionine sulfoxide.	SAM, methionine, cysteine, N-acetylcysteine, N-acetyltaurine, taurine, sulfo-L-alanine, methionine sulfoxide, N-acetylmethionine sulfoxide, N-acetylmethionine, S-methylcysteine-sulfoxide.	SAH, cystathionine, N-acetyltaurine, S-methylcysteine, taurine, methionine sulfone.
	Positive trend (p<0.10)	Not applicable.	S-methylcysteine.	S-methylcysteine sulfoxide.
	Insignificant change (p>0.1)	SAH, cysteine sulfinic acid.	SAH, cysteine sulfinic acid.	Methionine sulfoxide, methionine.
	Negative trend (p<0.10)	Not applicable.	Not applicable.	Not applicable.
	Significant negative trend (p<0.05)	Cystathionine, hypotaurine, N-formylmethionine.	Cystathionine, hypotaurine, N-formylmethionine.	N-formylmethionine, hypotaurine, cysteine, SAM, N-acetylcysteine, sulfo-L-alanine, N-acetylmethionine, cysteine sulfinic acid.
Gly-Ser-Thr Metabolism	Significant positive trend (p<0.05)	Threonine, glycine, betaine, serine, dimethylglycine, homoserinelactone, N-acetylglycine.	Betaine, glycine, serine, dimethylglycine, homoserinelactone, N-acetylglycine.	N-acetylserine, betaine, dimethylglycine, N-acetylglycine.
	Positive trend (p<0.10)	N-acetylserine.	Not applicable.	N-acetylthreonine.
	Insignificant change (p>0.1)	Phosphothreonine.	Threonine, phosphothreonine, N-acetylserine.	Threonine.
	Negative trend (p<0.10)	Not applicable.	Not applicable.	Phosphothreonine.
	Significant negative trend (p<0.05)	N-acetylthreonine.	N-acetylthreonine.	Glycine, serine, homoserinelactone.
Polyamine Metabolism	Significant positive trend (p<0.05)	Putrescine, MTA, N-acetylputrescine, 4-acetamidobutanoeate.	Putrescine, MTA, N-acetylputrescine, 4-acetamidobutanoeate.	4-acetamidobutanoate.
	Positive trend (p<0.10)	Not applicable.	Not applicable.	Not applicable.
	Insignificant change (p>0.1)	N-acetylspermidine, N-diacetylspermine.	N-acetylspermidine, N-diacetylspermine.	N-acetylspermidine.
	Negative trend (p<0.10)	Not applicable.	Not applicable.	Not applicable.

CONTINUE TABLE S3

	Significant negative trend (p<0.05)	Spermidine.	Spermidine.	Putrescine, spermidine, MTA, M-acetylputrescine, N-diacetylspermine.
Glutathione Metabolism	Significant positive trend (p<0.05)	2-hydroxybutyrate, GSSG, cysteine-glutathine disulfide, opthalmalate.	2-hydroxybutyrate, GSSG, opthalmalate, cysteine-glutathione disulfide.	2-hydroxybutyrate, 5-oxoproline, 4-hydroxynonenal-glutathione.
	Positive trend (p<0.10)	Not applicable.	Not applicable.	Not applicable.
	Insignificant change (p>0.1)	4-hydroxy-nonenal glutathione.	4-hydroxy-nonenal-glutathione.	Cysteine-glutathione disulfide, cysteinglycine.
	Negative trend (p<0.10)	Not applicable.	Not applicable.	Not applicable.
	Significant negative trend (p<0.05)	GSH, S-lactoylglutathione, S-methylglutathione, cysteinglycine, 5-oxoproline.	S-lactoylglutathione, S-methylglutathione, 5-oxoproline, GSH, cysteinglycine.	S-lactoylglutathione, GSSG, S-methylglutathione, GSH, opthalmalate.

Table S4. Identification of trends of one-carbon metabolites during the intermediate stage between steady-state of Mesenchymal Stem Cells (MSCs) and early transitional-states of differentiated counterparts. Statistical trends in the relative abundance of individual metabolites at the indicated times. Times selected by their potential overlap with the earliest/immediate transcriptional changes derived from the induction of differentiation. Experiments were from n=5 biological replicates.
Related to Figure 1 and descriptive of Supplemental figure 1F.

PATHWAYS	Comparisons	*Comparison of MSCs vs 6 hours of differentiation*	*Comparison of MSCs vs 24 hours of differentiation*	*Comparison of MSCs at 24 hours of differentiation vs 96 hours differentiation*
Methionine-SAM Metabolism	Significant positive trend (p<0.05)	Methionine, cysteine s-sulfate, SAM, taurine, methionine sulfoxide, hypotaurine, N-acetylmethionine sulfoxide.	Methionine, N-acetyltaurine, cystine, cysteine sulfinic acid, methionine sulfoxide.	Cystine, cysteine s-sulfate, methionine sulfoxide.
	Positive trend (p<0.10)	S-methylcysteine.	Cysteine s-sulfate.	Not applicable.
	Insignificant change (p>0.1)	SAH, cystine, cysteine sulfinic acid.	SAM, cysteine, taurine, hypotaurine.	SAM, methionine, DMPTA, N-acetylmethionine sulfoxide, S-methylcysteine, cysteine sulfinic acid, N-formylmethionine.
	Negative trend (p<0.10)	Not applicable.	N-formylmethionine.	N-acetylmethionine.
	Significant negative trend (p<0.05)	N-acetylmethionine, N-acetylcysteine, methionine sulfone, cysteine, N-acetyltaurine, DMPTA, N-formylmethionine.	N-acetylmethionine, N-acetylcysteine, DMPTA, S-methylcysteine, methionine sulfone, SAH, N-acetylmethionine sulfoxide.	N-acetylcysteine, methionine sulfone, cysteine, SAH, taurine, N-acetyltaurine, hypotaurine.
Gly-Ser-Thr Metabolism	Significant positive trend (p<0.05)	Threonine, N-acetylthreonine.	Threonine, N-acetylthreonine, glycine, serine, N-acetylserine.	N-acetylthreonine.
	Positive trend (p<0.10)	Glycine, serine.	Not applicable.	Not applicable.
	Insignificant change (p>0.1)	N-acetylserine.	Not applicable.	Threonine, Serine.
	Negative trend (p<0.10)	Not applicable.	Not applicable.	Not applicable.
	Significant negative trend (p<0.05)	Betaine, dimethylglycine.	Betaine, dimethylglycine.	Betaine, dimethylglycine, glycine, N-acetylserine.
Polyamine Metabolism	Significant positive trend (p<0.05)	MTA.	Putrescine, N-acetylspermidine.	Not applicable.
	Positive trend (p<0.10)	Not applicable.	N-acetylputrescine.	Not applicable.
	Insignificant change (p>0.1)	N-acetylspermidine, N-acetylputrescine, putrescine, spermine, spermidine.	Spermidine, Spermine.	Spermine, N-acetylputrescine, 4-acetamidobutanoate.
	Negative trend (p<0.10)	Not applicable.	MTA.	Not applicable.
	Significant negative trend (p<0.05)	4-acetamidobutanoeate.	4-acetamidobutanoeate.	Spermidine, N-acetylspermidine, MTA, putrescine.
Glutathione Metabolism	Significant positive trend (p<0.05)	CoA-glutathione, GSSG, 4-hydroxy-nonenal-glutathione, S-methylglutathione.	Cysteine glutathione-disulfide.	5-oxoproline.
	Positive trend (p<0.10)	Dicarboxyethylglutathione, cysteine glutathione-disulfide.	Not applicable.	Not applicable.
	Insignificant change (p>0.1)	Cysteinglycine, GSH, S-lactoylglutathione, 3-dephospho-CoA-glutathione.	Cysteinglycine, 5-oxoproline, S-lactoylglutathione.	CoA-glutathione, 3-dephospho-CoA-glutathione, 4-hydroxy-nonenal-glutathione, S-

CONTINUE TABLE S4

			methylglutathione, GSH, S-lactoylglutathione, dicarboxyethylglutathione.
Negative trend ($p<0.10$)	Not applicable.	Not applicable.	2-hydroxybutyrate.
Significant negative trend ($p<0.05$)	Ophtalmate, 5-oxoproline, 2-hydroxybutyrate.	Ophtalmate, CoA-glutathione, S-methylglutathione, 2-hydroxybutyrate, dicarboxyethyl glutathione, GSH, GSSG, 4-hydroxy-nonenal-glutathione, 3-dephospho-CoA-glutathione.	Ophtalmate, cysteinglycine, cysteine glutathione-disulfide, GSSG.

Table S5. Sequences of primers, where M for mouse, H for human.
Related to STAR Methods.

Gene name	Specie	Forward primer seq	Revers primer seq
Beta-Actin	M	CATTGCTGACAGGATGCAGAAGG	TGCTGGAAGGTGGACAGTGAGG
Gapdh	M	CATCACTGCCACCCAGAAGACTG	ATGCCAGTGAGCTTCCCGTTCAG
Nat1	M	ATTCTTCGTTGTCAAGCCGCCAAAGTGGAG	AGTTGTTTGCTGCGGAGTTGTCATCTCGTC
RPL38	M	AGGATGCCAAGTCTGTCAAGA	TCCTTGTCTGTGATAACCAGG
Ascl1	M	CTCGTCCTACTCCTCCGACG	ATCTGCTGCCATCCTGCTTC
Cd44	M	ACAACCCTTCAGCCTACTGC	CGCCGCTCTTAGTGCTAGAT
Cd9	M	CTGTGGCATAGCTGGTCCTTTG	AGACCTCACTGATGGCTTCAGG
cMyc	M	GTGCTGCATGAGGAGACACC	GACCTCTTGGCAGGGGTTTG
Klf4	M	GCACACCTGCGAACTCACAC	CCGTCCCAGTCACAGTGGTAA
Gfap	M	AGGTTGAATCGCTGGAGGAG	GCTTGGCCACATCCATCTC
Nes	M	CCAGAGCTGGACTGGAACTC	ACCTGCCTCTTTTGGTTCCT
Cd133	M	TCCCTCCTGTGCAGCAATCA	CCAAACTTCTTCGTTTCCCCGA
Sox2	M	AACGGCAGCTACAGCATGATGC	CGAGCTGGTCATGGAGTTGTAC
Hes5	M	CCGTCAGCTACCTGAAACACAG	GGTCAGGAACTGTACCGCCTC
Mtr	M	GCTCTGTGAAGACCTCATCTGG	GAGCCATTCCTCCACTCATCTG
Chrd1	M	GTATGCAGAGGGGATGCAGAA	TGGAGGATCGTAGGGGGAAC
Odc1	M	TGCCACACTCAAAACCAGCAGG	ACACTGCCTGAACGAAGGTCTC
Beta-III-tubulin	M	ACCTATTCAGGCCCGACAACTTTA	GCAGGCAGTCACAATTCTCACAC
Map2	M	CTGCGAGTAAGCTGTGACCG	AGCTGAGGAACCTTAATTCTTGCC
SB100	M	GACTCCAGCAGCAAAGGTGA	TGATTTCCTCCAGGAAGTGAGAG
Mat1a	M	CCTTCTCTGGAAAGGACTACACC	GACAGAGGTTCTGCCACACCAA
Ascl1	M	CGGAACTGATGCGCTGCAAACG	GGCAAAACCCAGGTTGACCAAC
Sox5	M	CGCCAGATGAAAGAGCAACTCAG	TGAGTCAGGCTCTCCAGTGTTG
Cd51	M	GTGTGAGGAACTGGTCGCCTAT	CCGTTCTCTGGTCCAACCGATA
Thy1	M	CCTTACCCTAGCCAACTTCACC	TTATGCCGCCACACTTGACCAG
Sox9	M	GCAGACCAGTACCCGCATCT	CTCGTTCAGCAGCCTCCAG
Aggrecan	M	CCTGCTACTTCATCGACCCC	AGATGCTGTTGACTCGAACCT
Col2a	M	AATGGGCAGAGGTATAAAGATAAGGA	CATTCCCAGTGTCACACACACA
Myf5	M	GGTGGAGAACTATTACAGCCTGC	ACAGTAGATGCTGTCAAAGCTGC
Ccnd1	M	GCAGAAGGAGATTGTGCCATCC	AGGAAGCGGTCCAGGTAGTTCA
Gdf6	M	CACTAGCTTTGTAGACAGAGGAC	CCTGGCGATAAAGCCTTAGCTC
Myh11	M	GCAACTACAGGCTGAGAGGAAG	TCAGCCGTGACCTTCTCTAGCT
Cldn2	M	AGGACTTCCTGCTGACATCCAG	AATCCTGGCAGAACACGGTGCA
Ckm	M	GGCTTCACTCTGGACGATGTCA	CCTTGAAGACCGTGTAGGACTC
Mef2c	M	GTGGTTTCCGTAGCAACTCCTAC	GGCAGTGTTGAAGCCAGACAGA
Vimentin	M	CGGAAAGTGGAATCCTTGCAGG	AGCAGTGAGGTCAGGCTTGGAA
Glast	M	GCGATTGGTCGCGGTGATAATG	CGACAATGACTGTCACGGTGTAC
Glutamine synthetase	M	CTGCCATACCAACTTCAGCACC	CTGGTGCCTCTTGCTCAGTTTG
Myelin Binding Protein	M	TCTGGCAAGGACTCACACAC	AGGTGGTGTTCGAGGTGTCA
O4	M	TGTAACAGGTCCTCGGAAGGG	TGTGCAAGGACAGGTTGTGAC
NSE	M	TGGCAAGGATGCCACTAACGTG	AACTCAGAGGCAGCCACATCCA
Synaptophysin	M	TTGGCTTCGTGAAGGTGCTGCA	ACTCTCCGTCTTGTTGGCACAC
CTCF	H	GGGCTTGAGAGCTGGGTTCTATT	CTTCGACTGCATCACCTTCCATT
NESTIN	H	GCACCTCAAGATGTCCCTCAGC	GTTTGCAGCCGGGAGTTCTCA
NEUROD1	H	TCACTGCTCAGGACCTACTAACAACA	GTCTGTCCAGCTTGGAGGACCTT
ASCL1	H	CGACTTCACCAACTGGTTCTGAG	TAAAGATGCAGGTTGTGCGATCA
CD44	H	CCAGAAGGAACAGTGGTTTGGC	ACTGTCCTCTGGGCTTGGTGTT
GUS B	H	GGTTTCACCAGGATCCACCTC	ACTCTCGTCGGTGACTGTTC
GAPDH	H	AATCCCATCACCATCTTCCA	TGGACTCCACGACGTACTCA
SOX2	H	CAAAAATGGCCATGCAGGTT	AGTTGGGATCGAACAAAAGCTATT
GFAP	H	AGAGATCCGCACGCAGTATG	GTAGTCGTTGGCTTCGTGCT
cMYC	H	GGATTCTCTGCTCTCCTCGAC	AGACTCTGACCTTTTGCCAGG

CONTINUE TABLE S5

CD133	H	CACTACCAAGGACAAGGCGTTC	CAACGCCTCTTTGGTCTCCTTG
OCT4	H	CCTGAAGCAGAAGAGGATCACC	AAAGCGGCAGATGGTCGTTTGG
KLF4	H	CATCTCAAGGCACACCTGCGAA	TCGGTCGCATTTTTGGCACTGG
NANOG	H	AAATACCTCAGCCTCCAGCAG	CCATTGCTATTCTTCGGCCAG
COL1A2	H	GGCCCTCAAGGTTTCCAAGG	CACCCTGTGGTCCAACAACTC